GEOTECHNICAL STABILITY ANALYSIS: NEW METHODS FOR AN OLD PROBLEM

Scott Sloan
Federation Fellow, Geotechnical Research Group, University of Newcastle

SUMMARY

Geotechnical stability analysis is traditionally performed by a variety of approximate methods that are based on the theory of limit equilibrium. Although they are simple and appeal to engineering intuition, these techniques suffer from a number of serious disadvantages, not the least of which is the need to presuppose an appropriate failure mechanism in advance. This feature can lead to inaccurate predictions of the true failure load, especially for realistic problems involving layered materials, complex loading, or three-dimensional deformation.

A much more rigorous method for assessing the stability of geostructures became available with the advent of the limit (or bound) theorems of classical plasticity in the 1950s. These theorems can be used to give upper and lower bounds on the predicted collapse load (a most valuable property in practice), do not require assumptions to be made about the mode of failure, and use only simple strength parameters that are familiar to geotechnical engineers. Although many ingenious bound results have been derived using analytical or numerical methods, practical application of the limit theorems has been restricted by the need to develop specific solution strategies for each problem. Over the last decade, the Newcastle Geotechnical Research Group has developed powerful new methods for performing stability analysis that combine the limit theorems with finite elements and optimisation. These methods are very general and can deal with layered soil profiles, anisotropic strength characteristics, complicated boundary conditions, and complex loading in both two and three dimensions. Indeed, they have already been used to obtain new stability solutions for a wide range of practical problems including soil anchors, slopes, foundations under combined loading, excavations, tunnels, mine workings, and sinkholes.

This paper gives an outline of the new techniques and considers a number of practical applications. Future research developments will also be highlighted.

1 STABILITY ANALYSIS

Stability analysis is used to predict the maximum load that a geostructure can support without failing. This load is known as the collapse load, the failure load, the limit load, or the ultimate load, and can be used to determine the allowable working load by dividing by a predetermined factor of safety. The precise value of the factor of safety depends on the geostructural application, with lower values being used for slopes and higher values being used for foundations. Rather than imposing a factor of safety on the limit load to obtain the allowable load, it is also possible to apply a factor of safety to the strength parameters for the geomaterial prior to performing the stability analysis.

Once the allowable load is known, the working settlements can be obtained using some form of settlement analysis (e.g. elastic analysis or nonlinear finite element analysis). In some cases, serviceability constraints on the deformations actually control the allowable load that can be imposed on a geostructure and, consequently, its load-carrying capacity is not fully utilised. Broadly speaking, there are four main methods for performing geotechnical stability analysis: limit equilibrium, limit analysis, slip-line methods, and the displacement finite element method. In this paper we will focus on the first two techniques.

1.1 LIMIT EQUILIBRIUM

Limit equilibrium is the oldest method for performing stability analysis and dates back to the time of Coulomb (1773). To estimate the limit load, this approach presupposes a failure mechanism and, typically, assumes that the stresses on the failure planes are limited by the traditional strength parameters c and ϕ. The chief advantages of the limit equilibrium method are its simplicity and long history of use. Its main disadvantage is the need to guess the shape of the failure surface in advance, with poor guesses giving poor estimates of the failure load. For many geotechnical problems the likely form of the failure surface is not intuitively obvious, especially if the problem has an irregular geometry, is subject to complicated loading, and involves layered or fractured media. Other shortcomings of the technique are (a) the resulting stresses do not satisfy equilibrium everywhere, (b) there is no simple means of checking the solution accuracy, (c) it is hard to incorporate anisotropy and inhomogeneity, and (d) it is difficult to generalise the procedure from two to three dimensions. To illustrate the key features of the limit equilibrium approach, we consider the classical problem of a smooth strip footing resting on a deep layer of undrained clay, as shown in Figure 1.

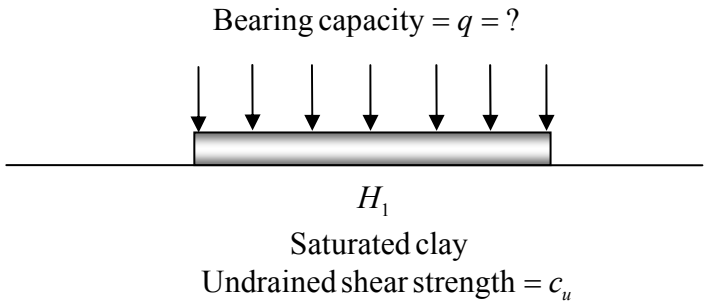

Figure 1 Smooth strip footing on deep layer of undrained clay

Let us first assume that failure occurs along a circular surface, whose centre is directly above the edge of the footing, as shown in Figure 2. Let us further assume that the undrained shear strength is fully mobilised along this failure surface at the point of collapse, so that $\tau = c_u$.

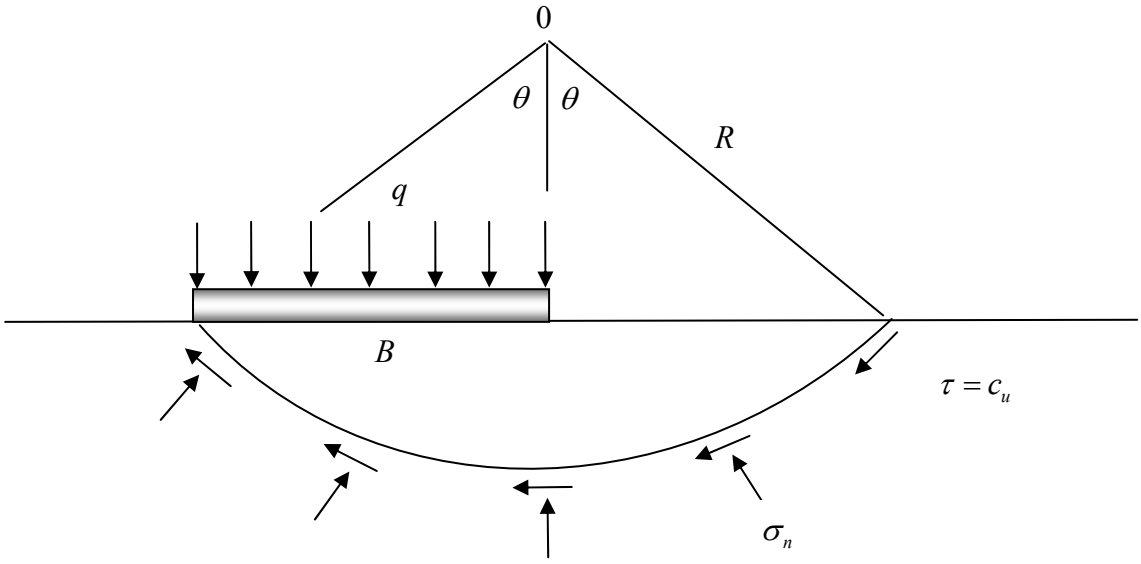

Figure 2 Limit equilibrium failure surface for strip footing

Taking moments about 0 we obtain

$$(qB)\times B/2 = (2R\theta \times c_u)\times R$$

or

$$q = 4c_u\theta / \sin^2\theta \tag{1}$$

The critical surface geometry is the one which gives the lowest value of q, so that

$$\frac{\mathrm{d}q}{\mathrm{d}\theta} = 4c_u\left(\frac{\sin^2\theta - 2\theta\sin\theta\cos\theta}{\sin^4\theta}\right) = 0$$

or

$$\tan\theta - 2\theta = 0$$

This simple nonlinear equation in θ can be solved to yield $\theta_{crit} = 66.8°$ which, after substituting in (1), furnishes

$$q = \frac{4\times c_u \times 66.8\times \pi}{180\times \sin^2(66.8)} = 5.52c_u \tag{2}$$

This value is about 7% above the well-known exact solution of $q = (2+\pi)c_u$ derived by Prandtl (1920).

1.2 LIMIT ANALYSIS

Limit analysis is based on the plastic bounding theorems developed by Drucker *et al*. (1951), and assumes small deformations, a perfectly plastic material [Figure 3(a)], and an associated flow rule [Figure 3(b)]. The latter assumption implies that the plastic strain rates $\dot{\varepsilon}_{ij}^p$ are normal to the yield surface $f(\sigma_{ij})$, so that $\dot{\varepsilon}_{ij}^p = \dot{\lambda}\partial f / \partial\sigma_{ij}$ where $\dot{\lambda}$ is a non-negative plastic multiplier rate (or plastic multiplier). Note that in plasticity theory it is necessary to work with velocities and strain rates, rather than displacements and strains, because the latter are undefined at collapse.

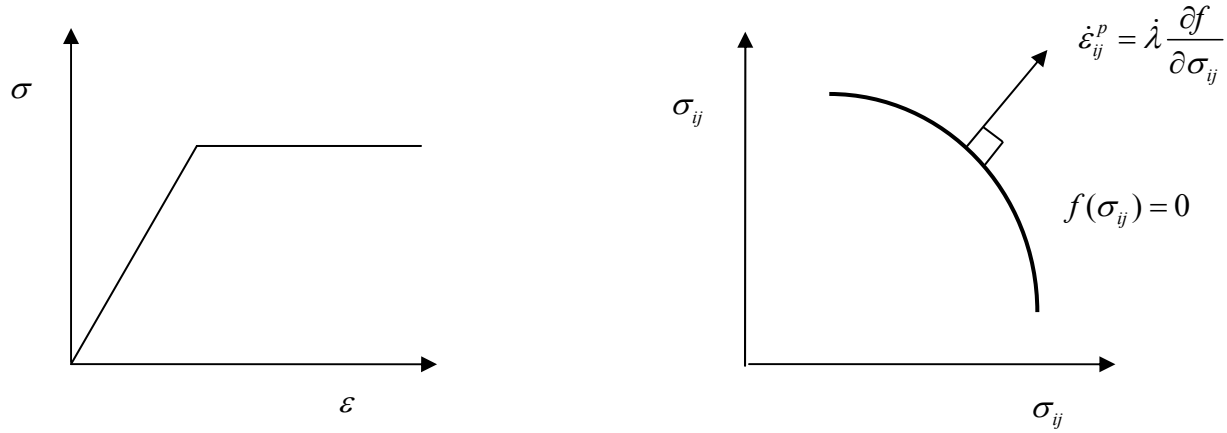

Figure 3 (a) Perfectly plastic material model and (b) associated flow rule

The lower bound theorem employs the notion of a *statically admissible stress field,* which is simply a stress field that satisfies equilibrium, the stress boundary conditions, and the yield criterion. For a perfectly plastic material model with an associated flow rule, it can be shown that the load carried by any statically admissible stress field is a lower bound on the true limit load. Although the limit

load for such a material is unique, the optimum stress field is not. This implies that it is possible to have a variety of stress fields that will give good lower bounds. To illustrate the application of lower bound limit analysis, we again consider the smooth rigid footing problem of Figure 1. The simple stress field shown in Figure 4, which consists of three distinct zones separated by two stress discontinuities, is statically admissible since it satisfies equilibrium, the stress boundary conditions, and the undrained (Tresca) yield criterion $\sigma_1 - \sigma_3 = 2c_u$. Note that each stress discontinuity is statically admissible because the normal and shear stresses are the same on both of its opposing sides, and that equilibrium is automatically satisfied everywhere in each zone because the unit weight is zero and the stress field is constant.

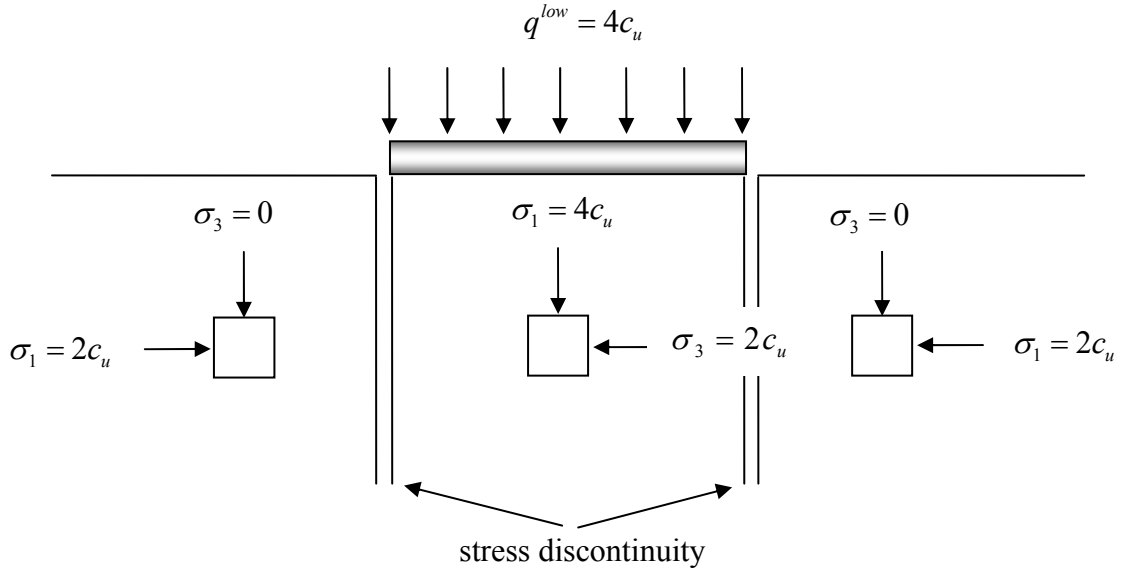

Figure 4 Lower bound stress field for strip footing

Since the vertical principal stress in the zone beneath the footing is $\sigma_1 = 4c_u$, the stress field gives a lower bound on the bearing capacity of $q^{low} = 4c_u$.

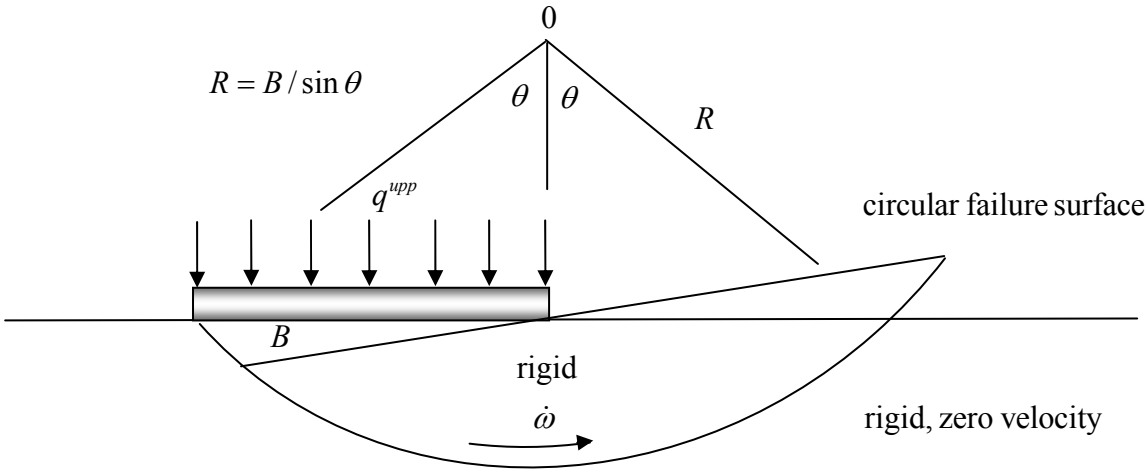

Figure 5 Upper bound failure mechanism for strip footing

The upper bound theorem employs the notion of a *kinematically admissible velocity field,* which is simply a velocity field that satisfies the velocity boundary conditions and the plastic flow rule. For such a field, it can be shown that an upper bound on the collapse load is obtained by equating the power expended by the external loads to the power dissipated internally by plastic deformation.

Note that although the true limit load from such a calculation is unique, the actual failure mechanism is not. A simple upper bound mechanism for our strip footing example is shown in Figure 5. For this case, failure is assumed to occur by rigid body rotation, with all the internal energy being dissipated along the velocity discontinuity. From the geometry of Figure 5, the rate of internal energy (or power) dissipation is

$$\dot{W}^{int} = P^{int} = \int \Delta u \; c_u \mathrm{d}L = (R \times \dot{\omega}) \times c_u \times (2R\theta)$$

where $\dot{\omega}$ is the angular velocity of the section about point 0 and Δu is the tangential velocity jump across the discontinuity. Equating this quantity to the rate of external work (or power) expended by the forces

$$\dot{W}^{ext} = P^{ext} = (q^{upp} \times B) \times (B/2 \times \dot{\omega})$$

and substituting for R gives

$$q^{upp} = 4c_u \theta / \sin^2 \theta$$

Setting $\mathrm{d}q/\mathrm{d}\theta = 0$ furnishes $\theta_{opt} = 66.8°$ and the optimal upper bound for this mechanism as

$$q^{upp} = 5.52c_u$$

Combining this result with the previous lower bound estimate we obtain

$$4c_u \le q \le 5.52c_u$$

Note that the limit equilibrium and upper bound calculations give the same estimate of the collapse load, but this is generally not the case for more complex failure mechanisms. Bearing in mind the limitations of the simple material model that they assume, the great attraction of the limit theorems is their ability to provide rigorous upper and lower bounds on the collapse load. This is a major advantage for complex practical problems where the failure load is difficult to estimate by other methods, and is one of the few instances in nonlinear computational mechanics where the error in the solution can be estimated directly. Although the limit theorems can be applied analytically to give useful bounds, numerical methods provide a more general means of harnessing their power and have become increasingly popular. Of the various numerical options available, finite element formulations have become the method of choice for practical applications and will be the focus of attention in this paper. These procedures inevitably result in some form of optimisation problem, the solution of which defines either a statically admissible stress field or a kinematically admissible velocity field. Finite element formulations of the limit theorems inherit all the advantages of the finite element method, and can model complex geometries, layered soils, discontinuities, complicated loadings, and a wide variety of boundary conditions. The key challenge, however, is to devise formulations and solution algorithms that are robust, efficient, and extendable to three dimensions.

The implicit assumption of an associated flow rule in the bound theorems has resulted in some debate on their suitability for frictional soils. Although it is well known that the use of an associated flow rule predicts excessive dilation during shear failure of such a soil, it is less clear whether this feature will have a major impact on the resulting limit load. Indeed, it can be argued that the flow rule will have a major influence on this quantity only if the problem is strongly constrained in a kinematic sense (Davis, 1968). For geomechanics problems which involve a freely deforming ground surface and a semi-infinite domain, the degree of kinematic constraint if often

low and it is reasonable to conjecture that the bound theorems will give good estimates of the true limit load. If we assume the plastic potential is convex and contained within the yield surface, we can quantify the effect of the flow rule more precisely by using the following results: (1) a conventional upper bound calculation gives a rigorous upper bound on the limit load for an equivalent material with a non-associated flow rule (Davis, 1968); and (2) a rigorous lower bound on the limit load for a non-associated material can be obtained by substituting the plastic potential for the yield criterion in the static admissibility conditions (Palmer, 1966). Although conceptually useful, the bounds so obtained can be far apart if the dilatancy angle is considerably less than the friction angle. In another approach, Drescher & Detournay (1993) suggest that limit loads for soils with non-associated flow rules can also be estimated by using rigid block mechanisms with reduced discontinuity strengths. These reduced strengths are functions of the friction and dilatancy angles, and follow the formulas derived by Davis (1968).

2 PROBLEM DEFINITION

Consider a body of volume V and boundary area A as shown in Figure 1. Let $\mathbf{t}$ and $\mathbf{q}$ denote, respectively, a set of fixed surface stresses (or tractions) acting on the boundary A_t and a set of unknown tractions acting on the boundary A_q. Similarly, define $\mathbf{g}$ and $\mathbf{h}$ to be a system of fixed and unknown body forces acting over the volume V.

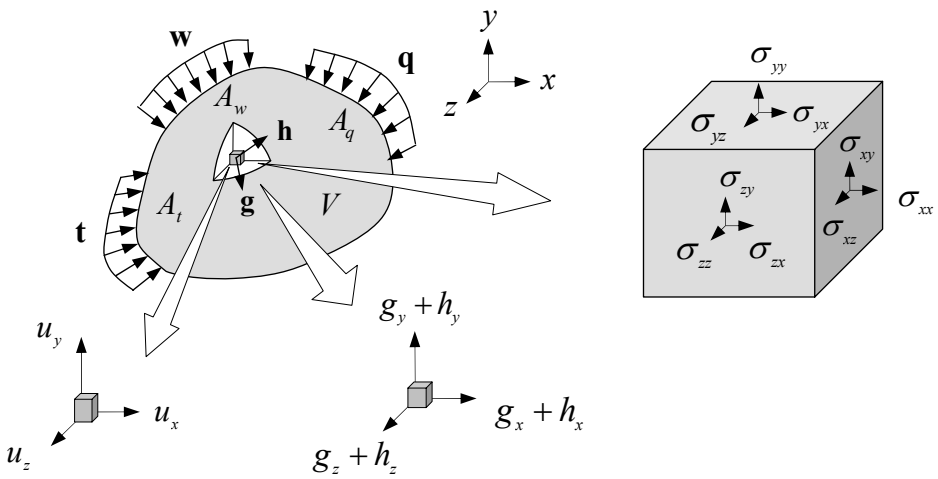

In a lower bound calculation we seek a stress distribution $\boldsymbol{\sigma} = \{\sigma_{xx}, \sigma_{yy}, \sigma_{zz}, \tau_{xy}, \tau_{yz}, \tau_{xz}\}^{\mathrm{T}}$ which satisfies equilibrium throughout V, balances the prescribed tractions $\mathbf{t}$ on A_t, nowhere violates the yield criterion f so that $f(\boldsymbol{\sigma}) \le 0$, and maximises the collapse load

$$Q = \int_{A_q} \mathbf{q}\, \mathrm{d}A + \int_V \mathbf{h}\, \mathrm{d}V$$

In an upper bound calculation we search for a velocity distribution $\mathbf{u} = \{u_x, u_y, u_z\}^{\mathrm{T}}$ which satisfies compatibility, the flow rule, the velocity boundary conditions $\mathbf{w}$ on the surface area A_w, and minimises the internal power dissipation defined by

$$P^{int} = \int \boldsymbol{\sigma}^{\mathrm{T}} \dot{\boldsymbol{\varepsilon}}^{p} \mathrm{d}V$$

where $\dot{\boldsymbol{\varepsilon}}^{p} = \{\dot{\varepsilon}_{xx}, \dot{\varepsilon}_{yy}, \dot{\varepsilon}_{zz}, \dot{\gamma}_{xy}, \dot{\gamma}_{yz}, \dot{\gamma}_{xz}\}^{\mathrm{T}}$ are the plastic strain rates. An upper bound on the limit load is then found by equating P^{int} to the power expended by the external loads, which may be written as

$$P^{ext} = \int_{A_t} \mathbf{t}^{\mathrm{T}} \mathbf{u}\, \mathrm{d}A + \int_{A_q} \mathbf{q}^{\mathrm{T}} \mathbf{u}\, \mathrm{d}A + \int_V \mathbf{g}^{\mathrm{T}} \mathbf{u}\, \mathrm{d}V + \int_V \mathbf{h}^{\mathrm{T}} \mathbf{u}\, \mathrm{d}V$$

To compute rigorous bounds on the collapse load, the body is discretised using linear finite elements. The resulting upper and lower bound solutions can be compared directly to give the mesh discretisation error, which is a major benefit in practical applications where the exact solution is unknown and hard to estimate using conventional methods. To give the best possible bounds, kinematically admissible velocity discontinuities and statically admissible stress discontinuities are incorporated at all inter-element boundaries for the two types of analyses. These discontinuities compensate for the use of low order elements and prevent the well-known phenomenon of 'locking' for undrained (incompressible) soil models in upper bound calculations. Rather than considering formulations based on yield surface linearisation and linear optimisation, we will now describe techniques that employ the native yield function and nonlinear optimisation. These methods are not only efficient for two and three-dimensional geometries, but also allow very general types of yield criteria to be considered.

3 FINITE ELEMENT LOWER BOUND FORMULATION

We now outline a finite element lower bound formulation proposed by Lyamin & Sloan (2002a), with some new modifications for handling stress discontinuities. This procedure has proved very successful in large-scale practical applications, and is being developed for commercial release. The linear elements used to compute the statically admissible stress field are shown in Figure 6.

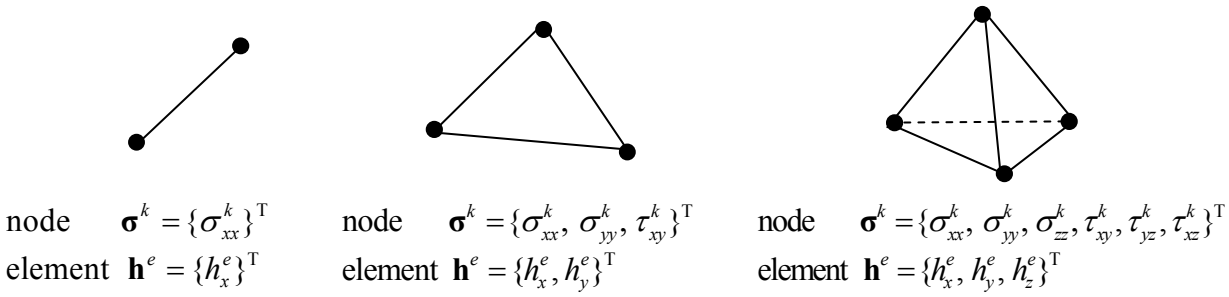

Figure 6 Linear elements for lower bound limit analysis

The lower bound procedure is formulated as a nonlinear optimisation problem, where the nodal stresses and/or element body forces are the unknowns and the objective function to be maximised corresponds to the collapse load. The unknowns are subject to equilibrium equality constraints for each continuum element, equilibrium equality constraints for each discontinuity, stress boundary conditions, and a yield condition inequality constraint for each node. Each of these aspects is now briefly described for the two-dimensional case (similar relations can be developed for three dimensions).

3.1 OBJECTIVE FUNCTION

The objective function corresponds to a force (the collapse load) which is to be maximised. The common case of optimising the normal and shear load along a boundary segment in two-dimensions is shown in Figure 7.

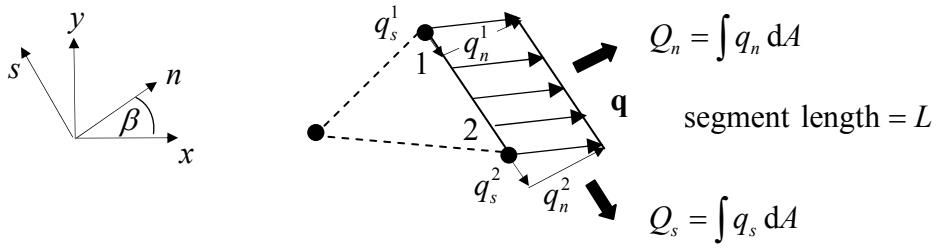

Figure 7 Optimising the load along a boundary

Since the stresses vary linearly, the normal and shear loads on an element edge of length L are given by

$$\begin{Bmatrix} Q_n \\ Q_s \end{Bmatrix} = \frac{L}{2}\left(\begin{Bmatrix} q_n^1 \\ q_s^1 \end{Bmatrix} + \begin{Bmatrix} q_n^2 \\ q_s^2 \end{Bmatrix} \right)$$

where the local surface stresses q_n and q_s can be expressed in terms of the Cartesian stresses at node k using the standard transformation equations

$$\begin{Bmatrix} q_n^k \\ q_s^k \end{Bmatrix} = \begin{bmatrix} \cos^2\beta & \sin^2\beta & \sin 2\beta \\ -\frac{1}{2}\sin 2\beta & \frac{1}{2}\sin 2\beta & \cos 2\beta \end{bmatrix} \begin{Bmatrix} \sigma_{xx}^k \\ \sigma_{yy}^k \\ \tau_{xy}^k \end{Bmatrix} \tag{3}$$

When summed over each loaded boundary edge, the contributions Q_n and Q_s give the total force which is to be maximised for the whole structure. In the case of body force loading, which is most often due to unit weight, the objective function contribution for each element is merely the body force component times the element volume.

3.2 CONTINUUM EQUILIBRIUM

Over each two-dimensional element, the stresses vary according to the relations

$$\boldsymbol{\sigma} = \sum_{k=1}^{3} N^k \boldsymbol{\sigma}^k \tag{4}$$

where N^k are the shape functions at some node k. After substituting these into the standard equilibrium equations for a solid

$$\begin{aligned} \frac{\partial \sigma_{xx}}{\partial x} + \frac{\partial \tau_{xy}}{\partial y} + h_x + g_x = 0 \\ \frac{\partial \sigma_{yy}}{\partial y} + \frac{\partial \tau_{xy}}{\partial x} + h_y + g_y = 0 \end{aligned} \tag{5}$$

we obtain two equality constraints for each element. When summed over all elements in the mesh, these define the global equilibrium constraints for the mesh.

3.3 DISCONTINUITY EQUILIBRIUM

To improve the accuracy of the computed collapse load, stress discontinuities are permitted at all edges that are shared by adjacent elements. Figure 8 illustrates such a stress discontinuity positioned between the edges of two adjacent triangles.

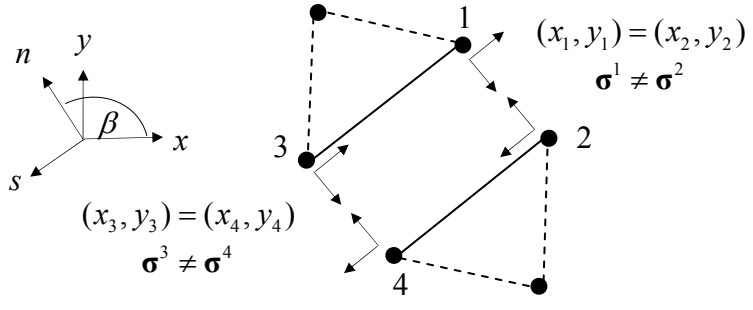

Figure 8 Statically admissible stress discontinuity

To satisfy equilibrium, and therefore be statically admissible, the normal and shear stresses must be the same on both sides of the discontinuity according to the relations

$$\begin{Bmatrix} \sigma_{nn}^1 \\ \tau_{ns}^1 \end{Bmatrix} = \begin{Bmatrix} \sigma_{nn}^2 \\ \tau_{ns}^2 \end{Bmatrix} \quad , \quad \begin{Bmatrix} \sigma_{nn}^3 \\ \tau_{ns}^3 \end{Bmatrix} = \begin{Bmatrix} \sigma_{nn}^4 \\ \tau_{ns}^4 \end{Bmatrix} \tag{6}$$

where for some node k

$$\begin{Bmatrix} \sigma_{nn}^k \\ \tau_{ns}^k \end{Bmatrix} = \begin{bmatrix} \cos^2\beta & \sin^2\beta & \sin 2\beta \\ -\frac{1}{2}\sin 2\beta & \frac{1}{2}\sin 2\beta & \cos 2\beta \end{bmatrix} \begin{Bmatrix} \sigma_{xx}^k \\ \sigma_{yy}^k \\ \tau_{xy}^k \end{Bmatrix} \tag{7}$$

Thus each pair of nodes on a stress discontinuity imposes two equilibrium equality constraints on the associated nodal stresses. Summing over all nodal pairs on the discontinuities gives the global set of discontinuity equilibrium constraints. Recently, Krabbenhøft *et al*. (2005) proposed a simple and elegant technique for modelling discontinuities in the upper bound method which is also applicable to the lower bound method (Lyamin *et al*., 2005). The basic idea, illustrated for the two-dimensional case in Figure 9, is to model each stress discontinuity by a patch of standard continuum elements and collapse certain nodal pairs to the same coordinates.

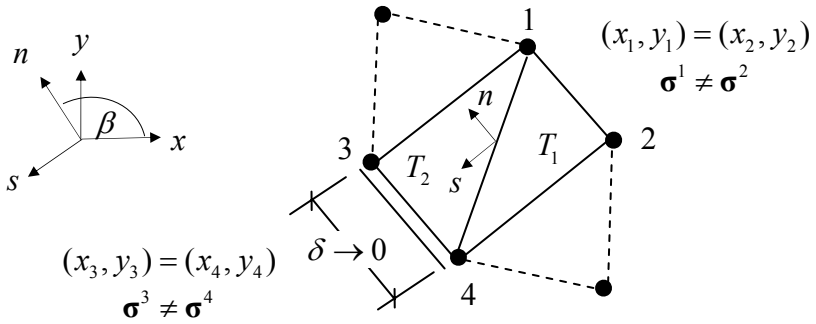

Figure 9 Patch-based stress discontinuity

Lyamin *et al*. (2005) show that using Equations (4) and (5) to impose the standard equilibrium conditions over triangles T_1 and T_2, and setting $(x_1, y_1) = (x_2, y_2)$ and $(x_3, y_3) = (x_4, y_4)$, leads to the equilibrium relations (6). Thus the normal and shear stresses are continuous across the discontinuity, but the tangential stress σ_{ss} can jump. This type of formulation permits discontinuities to be modelled using standard continuum elements and is very simple to implement.

3.4 STRESS BOUNDARY CONDITIONS

To satisfy equilibrium, the transformed stresses for any boundary node must match the prescribed surface stresses $\mathbf{t}$.

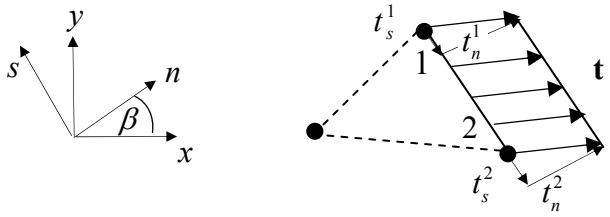

Figure 10 Stress boundary conditions

With reference to Figure 10, this requirement may be expressed by the equations

$$\begin{Bmatrix} \sigma_{nn}^1 \\ \tau_{ns}^1 \end{Bmatrix} = \begin{Bmatrix} t_n^1 \\ t_s^1 \end{Bmatrix} \quad , \quad \begin{Bmatrix} \sigma_{nn}^2 \\ \tau_{ns}^2 \end{Bmatrix} = \begin{Bmatrix} t_n^2 \\ t_s^2 \end{Bmatrix}$$

where $\{\sigma_{nn}^k , \tau_{ns}^k\}^{\mathrm{T}}$ for node k are again given by equation (7). These constraints are applied to all edges where surface stresses are prescribed.

3.5 YIELD CONDITIONS

Since the stresses are assumed to vary linearly over an element, the yield condition $f(\boldsymbol{\sigma})$ will be satisfied at every point if we impose the inequality constraint $f(\boldsymbol{\sigma}^k) \le 0$ for each node k. In the two-dimensional case, this implies that the nodal stresses for each element are subject to three nonlinear inequality constraints.

3.6 LOWER BOUND NONLINEAR OPTIMISATION PROBLEM

Summing the objective function coefficients and constraints for a given mesh leads to a nonlinear optimisation problem where the unknowns are stresses and body loads. Let $\mathbf{c}_1$ and $\mathbf{c}_2$ denote global vectors of objective function coefficients, $\boldsymbol{\sigma}$ denote a global vector of unknown nodal stresses, $\mathbf{h}$ denote a global vector or element body forces (unit weights), $\mathbf{c}_1^{\mathrm{T}}\boldsymbol{\sigma} + \mathbf{c}_2^{\mathrm{T}}\mathbf{h}$ denote the collapse load, $\mathbf{A}$ denote matrices of equality constraint coefficients, $\mathbf{b}$ denote vectors of coefficients, and $f_k(\boldsymbol{\sigma})$ denote the yield function at node k. The optimisation problem for the finite element lower bound then takes the form

$$\begin{array}{lr} \text{Objective function} & \\ \quad \text{Maximise collapse load} & \max(\mathbf{c}_1^{\mathrm{T}}\boldsymbol{\sigma} + \mathbf{c}_2^{\mathrm{T}}\mathbf{h}) \\ \text{Subject to} & \\ \quad \text{Continuum equilibrium} & \mathrm{A}_{11}\boldsymbol{\sigma} + \mathrm{A}_{12}\mathbf{h} = \mathbf{b}_1 \\ \quad \text{Discontinuity equilibrium} & \mathrm{A}_2\boldsymbol{\sigma} = \mathbf{b}_2 \\ \quad \text{Stress boundary conditions} & \mathrm{A}_3\boldsymbol{\sigma} = \mathbf{b}_3 \\ \quad \text{Yield condition for each node k} & f_k(\boldsymbol{\sigma}^k) \le 0 \end{array} \tag{8}$$

The solution to the nonlinear programming problem (8), which constitutes a statically admissible stress field, can be found efficiently by solving the system of nonlinear equations that define its Kuhn-Tucker optimality conditions. The two-stage quasi-Newton solver designed by Lyamin (1999) and Lyamin & Sloan (2002a) for this purpose usually requires less than about 50 iterations, regardless of the problem size. Because it does not require the yield surface to be linearised, this type of lower bound formulation can be extended to three dimensions and used with a wide range of yield criteria.

4 A FINITE ELEMENT UPPER BOUND FORMULATION

We now outline the finite element upper bound formulation first proposed by Lyamin & Sloan (2002b), with a new patch-based method for modelling velocity discontinuities (Krabbenhøft *et al*., 2005). This procedure, which is the first to incorporate velocity discontinuities in three dimensions with general types of yield criteria, is applicable to large-scale problems and is also being

commercialised. The elements used to compute the kinematically admissible velocity field, shown in Figure 11, use a linear variation of the velocities and constant stresses.

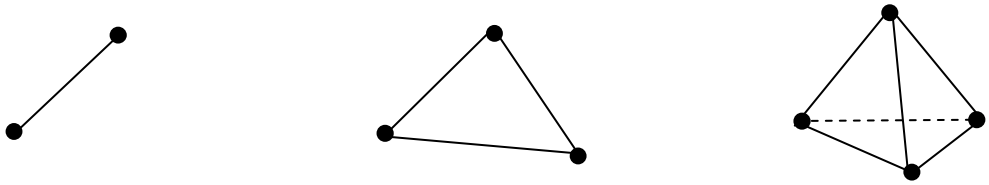

node $\mathbf{u}^k = \{u_x^k\}^{\mathrm{T}}$ element $\boldsymbol{\sigma}^e = \{\sigma_{xx}^e\}^{\mathrm{T}}$

node $\mathbf{u}^k = \{u_x^k, u_y^k\}^{\mathrm{T}}$ element $\boldsymbol{\sigma}^e = \{\sigma_{xx}^e, \sigma_{yy}^e, \tau_{xy}^e\}^{\mathrm{T}}$

node $\mathbf{u}^k = \{u_x^k, u_y^k, u_z^k\}^{\mathrm{T}}$ element $\boldsymbol{\sigma}^e = \{\sigma_{xx}^e, \sigma_{yy}^e, \sigma_{zz}^e, \tau_{xy}^e, \tau_{yz}^e, \tau_{xz}^e\}^{\mathrm{T}}$

Figure 11 Linear elements for upper bound limit analysis

The upper bound procedure is formulated as a nonlinear optimisation problem, where nodal velocities and element stresses are the unknowns and the objective function to be minimised is the internal power dissipation. To satisfy the requirements of the upper bound theorem, the unknowns are subject to constraints arising from the flow rule, the velocity boundary conditions, and the yield condition. Each of these aspects is now briefly described for the two-dimensional case (similar relations can be developed for three dimensions).

4.1 OBJECTIVE FUNCTION

In the finite element upper bound formulation the objective function corresponds to the internal dissipated power. This quantity is minimised and equated to the work expended by the external loads to give the limit load. Noting that the stresses and plastic strain rates are constant over each element, and summing over all the elements, the internal power dissipation may be written as

$$P^{int} = \int \boldsymbol{\sigma}^{\mathrm{T}} \dot{\boldsymbol{\varepsilon}}^p \mathrm{d}V = \sum_e (\boldsymbol{\sigma}^{\mathrm{T}} \dot{\boldsymbol{\varepsilon}}^p V)^e \tag{9}$$

For each element there exists a matrix $\mathbf{B}^e$ that relates the (constant) plastic strain rates to the nodal velocities according to

$$\dot{\boldsymbol{\varepsilon}}^p = \frac{1}{V^e} \mathbf{B}^e \mathbf{u}^e \tag{10}$$

$\mathbf{B}^e$ is the strain-displacement matrix from conventional finite element analysis, multiplied by the element volume. Inserting Equation (10) into Equation (9) gives the total internal dissipated power for the mesh, in terms of the unknowns stresses and velocities, as

$$P^{int} = \boldsymbol{\sigma}^{\mathrm{T}} \mathbf{B} \mathbf{u}$$

where $\boldsymbol{\sigma}$ is a global vector of element stresses, $\mathbf{u}$ is a global vector of nodal velocities, and $\mathbf{B} = \sum_e \mathbf{B}^e$.

4.2 CONTINUUM FLOW RULE

To be kinematically admissible, and thus give an upper bound on the limit load, the velocity field must satisfy the constraints imposed by an associated flow rule. For a two dimensional element, the flow rule conditions may be written as

$$\dot{\varepsilon}^p_{xx} = \dot{\lambda}\partial f / \partial \sigma_{xx}$$
$$\dot{\varepsilon}^p_{yy} = \dot{\lambda}\partial f / \partial \sigma_{yy}, \quad \dot{\lambda} \geq 0, \quad \dot{\lambda} f(\boldsymbol{\sigma}^e) = 0$$
$$\dot{\gamma}^p_{xy} = \dot{\lambda}\partial f / \partial \tau_{xy}$$

or

$$\dot{\boldsymbol{\varepsilon}}^p = \dot{\lambda}\nabla f(\boldsymbol{\sigma}^e), \quad \dot{\lambda} \geq 0, \quad \dot{\lambda} f(\boldsymbol{\sigma}^e) = 0 \tag{11}$$

where $\dot{\lambda}$ is the plastic multiplier. Combining Equations (10) and (11), the flow rule constraints for each element may be expressed as

$$\mathbf{B}^e \mathbf{u}^e = \dot{\alpha}\nabla f(\boldsymbol{\sigma}^e), \quad \dot{\alpha} \geq 0, \quad \dot{\alpha} f(\boldsymbol{\sigma}^e) = 0 \tag{12}$$

where $\dot{\alpha} = V^e \dot{\lambda}$. Thus, for the two-dimensional case, the flow rule generates four equality constraints and one inequality constraint on the velocity field per element. Since the yield function is not linearised, all the equality constraints are generally nonlinear.

4.3 DISCONTINUITY FLOW RULE

Velocity discontinuities can be incorporated using the patch-based formulation of Krabbenhøft *et al.* (2005). The concept behind this procedure is identical to that discussed previously for the lower bound method, with each discontinuity being modelled by a collapsed patch of standard continuum elements. For the two-dimensional case, shown in Figure 12, each discontinuity comprises two triangles and has 6 unknown stresses.

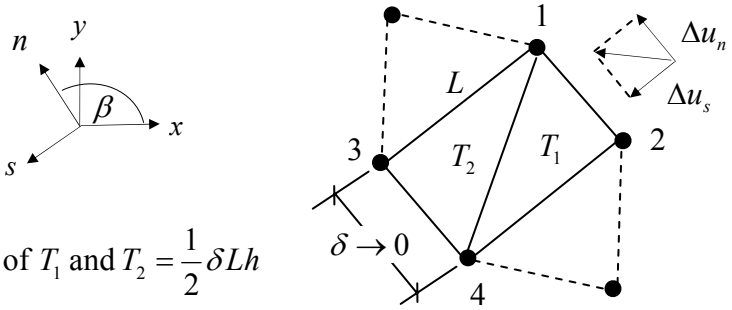

Volume of T_1 and $T_2 = \frac{1}{2}\delta Lh$

Figure 12 Patch-based velocity discontinuity

If we let the discontinuity width $\delta \to 0$, it may be shown (Krabbenhøft *et al.*, 2005) that the local strains in each triangle approach the following values

$$\begin{aligned} \dot{\varepsilon}^p_{ss} &\to 0 \\ \dot{\varepsilon}^p_{nn} &\to \Delta u_n / \delta \\ \dot{\gamma}^p_{ns} &\to \Delta u_s / \delta \end{aligned} \tag{13}$$

where $(\Delta u_n, \Delta u_s)$ are finite velocity jumps in the normal and tangential directions which are related to the Cartesian velocity jumps by

$$\begin{Bmatrix} \Delta u_n \\ \Delta u_s \end{Bmatrix} = \begin{bmatrix} \cos\beta & \sin\beta \\ -\sin\beta & \cos\beta \end{bmatrix} \begin{Bmatrix} \Delta u_x \\ \Delta u_y \end{Bmatrix}$$

From Equation (13) we see that the strains become infinite as $\delta \to 0$, but the strains times the element volume remain finite according to

$$\begin{aligned} \dot{\varepsilon}_{ss}^{p} \times V^{e} &= 0 \\ \dot{\varepsilon}_{nn}^{p} \times V^{e} &= \frac{\Delta u_n}{\delta} \times \frac{1}{2} \delta L h = \Delta u_n L h / 2 \\ \dot{\gamma}_{ns}^{p} \times V^{e} &= \frac{\Delta u_s}{\delta} \times \frac{1}{2} \delta L h = \Delta u_s L h / 2 \end{aligned} \tag{14}$$

where h is the out-of-plane element thickness. The above relations confirm that discontinuous velocity jumps can be modelled by merely imposing the flow rule constraints (12) over each triangle and setting $(x_1, y_1) = (x_2, y_2)$ and $(x_3, y_3) = (x_4, y_4)$. This allows discontinuity elements to be treated in exactly the same way as continuum elements and is simple to implement. Moreover, it is extendable to three dimensions and permits general types of yield criteria to be modelled.

4.4 VELOCITY BOUNDARY CONDITIONS

As shown in Figure 13, the transformed velocities must match the prescribed velocities for any boundary node.

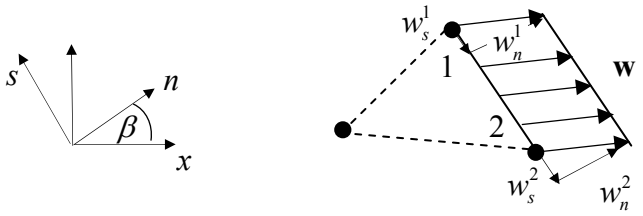

Figure 13 Velocity boundary conditions

In two dimensions, this requirement may be expressed by four equality constraints

$$\begin{Bmatrix} u_n^1 \\ u_s^1 \end{Bmatrix} = \begin{Bmatrix} w_n^1 \\ w_s^1 \end{Bmatrix} \quad , \quad \begin{Bmatrix} u_n^2 \\ u_s^2 \end{Bmatrix} = \begin{Bmatrix} w_n^2 \\ w_s^2 \end{Bmatrix}$$

where, for some node k, the transformed nodal velocities are given by standard relations

$$\begin{Bmatrix} u_n^k \\ u_s^k \end{Bmatrix} = \begin{bmatrix} \cos\beta & \sin\beta \\ -\sin\beta & \cos\beta \end{bmatrix} \begin{Bmatrix} u_x^k \\ u_y^k \end{Bmatrix}$$

These constraints must be applied to all boundary nodes that have prescribed velocities.

4.5 YIELD CONDITIONS

The yield condition $f(\boldsymbol{\sigma})$ can be satisfied at every point in the mesh if we impose the inequality constraint $f(\boldsymbol{\sigma}^e) \le 0$ for each element e. In two-dimensions, this implies that the stresses for each triangular element are subject to one nonlinear inequality constraint.

4.6 UPPER BOUND NONLINEAR OPTIMISATION PROBLEM

After assembling the objective function coefficients and constraints for a mesh, the upper bound nonlinear optimisation problem can be expressed as

$$
\begin{aligned}
&\text{Objective function} \\
&\quad \text{Minimise dissipated power} && \min \boldsymbol{\sigma}^{\mathrm{T}} \mathbf{B}\mathbf{u} \\
&\text{Subject to} \\
&\quad \text{Flow rule} && \mathbf{B}\mathbf{u} = \sum_e \dot{\alpha}^e \nabla f(\boldsymbol{\sigma}^e) \\
& && \dot{\alpha}^e \geq 0 \\
& && \dot{\alpha}^e f(\boldsymbol{\sigma}^e) = 0 \\
&\quad \text{Velocity boundary conditions} && \mathbf{A}\mathbf{u} = \mathbf{b} \\
&\quad \text{Yield condition for each element } e && f(\boldsymbol{\sigma}^e) \leq 0
\end{aligned}
\tag{15}
$$

where $\boldsymbol{\sigma}$ is a global vector of unknown element stresses, $\mathbf{u}$ is a global vector of unknown nodal velocities, $\mathbf{B}$ is a global compatibility matrix, $\boldsymbol{\sigma}^{\mathrm{T}} \mathbf{B}\mathbf{u}$ is the dissipated power, $\mathbf{A}$ is a matrix of equality constraint coefficients, $\mathbf{b}$ is a known vector of coefficients, $\dot{\alpha}^e$ is the plastic multiplier times the volume for element e, and $f(\boldsymbol{\sigma}^e)$ is the yield function for element e. The solution to Equation (15) constitutes a kinematically admissible velocity field and can be found efficiently by treating the system of nonlinear equations that define the Kuhn-Tucker optimality conditions. Interestingly, these optimality conditions do not involve $\dot{\alpha}^e$, so these quantities do not need to be included as unknowns. The two-stage quasi-Newton solver proposed by Lyamin (1999) and Lyamin & Sloan (2002b) usually requires less than about 50 iterations, regardless of the problem size, and results in a very efficient formulation.

5 KEY FEATURES OF FINITE ELEMENT LIMIT ANALYSIS

The upper and lower bound methods described in the preceding sections have a number of important advantages that make them very attractive for geotechnical analysis. These include:

(1) The limit load is given directly, without the need to perform a complete incremental analysis. This is a major advantage in large scale three-dimensional applications, where stability analysis using the conventional finite element method is both difficult and time consuming.

(2) For the material model assumed, the loads obtained are rigorous upper and lower bounds on the true collapse load. This means that the difference between the bounds gives a direct measure of the mesh discretisation error in the solution. For many practical problems it is often sufficient to base a design on the lower bound solution, with the upper bound solution providing an accuracy check as well as insight into the failure mechanism.

(3) Apart from providing an accuracy check, the bounding property of the methods provides some insurance against operator error.

(4) The methods can handle complex boundary and loading conditions, as well as anisotropic and inhomogeneous soil properties.

(5) No assumptions are needed in advance about the shape of the failure surface (unlike limit equilibrium calculations).

(6) The methods permit discontinuities in the stress and velocity fields. This means that they can model jointed media and soil-structure interfaces in a natural manner. It also means that, even with a modest number of elements, the computed solutions are often quite accurate.

(7) Compared with the traditional incremental finite element method, the procedures are very fast and straightforward to use.

6 IMPLICATIONS OF AN ASSOCIATED FLOW RULE

For a Mohr-Coulomb material the strength is governed by the cohesion c' and friction angle ϕ', while the volume change during plastic shearing is controlled by the dilatancy angle ψ'. With an associated flow rule we assume $\psi' = \phi'$, whereas for a real soil we often observe that $\psi' < \phi'$. Figure 14 shows the dilation predicted by these two different assumptions for plastic shearing along a planar failure surface. For the same shear displacement increment (velocity jump) Δu_s, the associated flow rule case gives a larger normal displacement increment (velocity jump) Δu_n, and hence a larger volume change in the material.

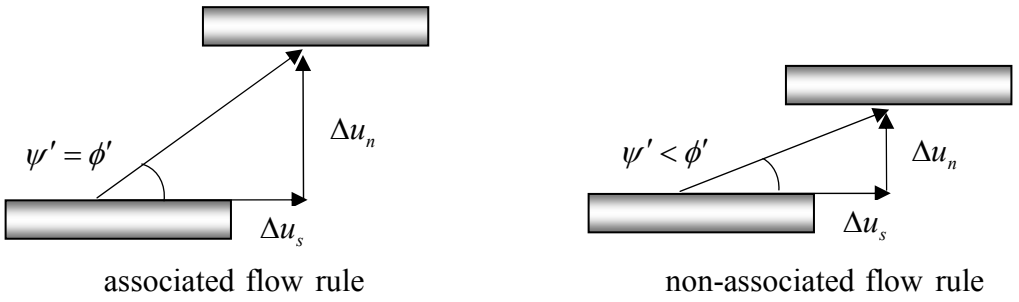

associated flow rule non-associated flow rule

Figure 14 Dilation during shearing on a planar failure surface

Defining tensile strains as positive, it may be shown that, under a general state of stress, the volumetric plastic strain rate is related to the maximum principal strain rate by the relation $\dot{\varepsilon}_v^p = (\tan^2(45° + \psi'/2) - 1)\dot{\varepsilon}_1^p$. This implies that, for a plot of $\dot{\varepsilon}_v^p$ versus $\dot{\varepsilon}_1^p$, the slope is zero when $\psi' = 0$ and greater than zero when $\psi' > 0$. The limitations of an associated flow rule are shown in Figure 15, which illustrates typical results for drained triaxial tests on real soils.

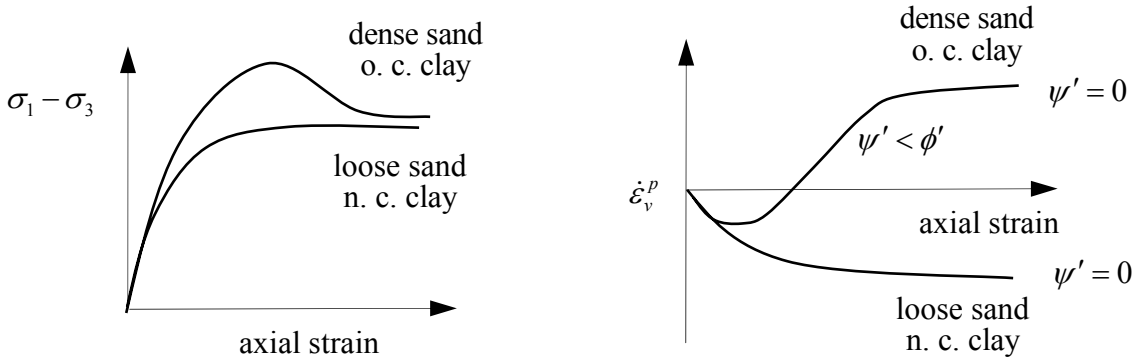

Figure 15 Drained triaxial test behaviour of real soils

Note that the flow rule is of little consequence for undrained soil behaviour, where all plastic deformation takes place at constant volume ($\psi_u = \phi_u = 0$). For drained behaviour, however, the implicit assumption of an associated flow rule in the bound theorems causes frequent debate about their suitability for predicting limit loads. Although the use of an associated flow rule predicts excessive dilation during shear failure of frictional soils, it is unclear whether this feature will have a major impact on the resulting limit load. Davis (1968) argued that the flow rule will have a major influence on this quantity only if the problem is strongly constrained in a kinematic sense. For problems which involve a stress-free ground surface and a semi-infinite domain, the degree of kinematic constraint is often low and it is reasonable to conjecture that the bound theorems will give good estimates of the true limit load. This conclusion is supported by the fact that, for many practical examples, identical limit loads can be obtained from very different failure mechanisms.

To illustrate the influence of the flow rule on the collapse load, consider the drained compression of a plane strain block of length L and diameter D, shown in Figure 16. Provided $L/D > \tan(45° + \psi'/2)$, an inclined failure plane is free to form across the specimen and the exact collapse pressure is given by $q_u = 2c' \tan(45° + \phi'/2)$. For a shorter specimen with $L/D = 1$, finite element limit analysis with an extremely fine mesh (4096 elements, 12288 nodes, 6086 discontinuities) and an associated flow rule gives lower and upper bounds on the exact collapse pressure as $4.47c' \le q_u \le 4.55c'$.

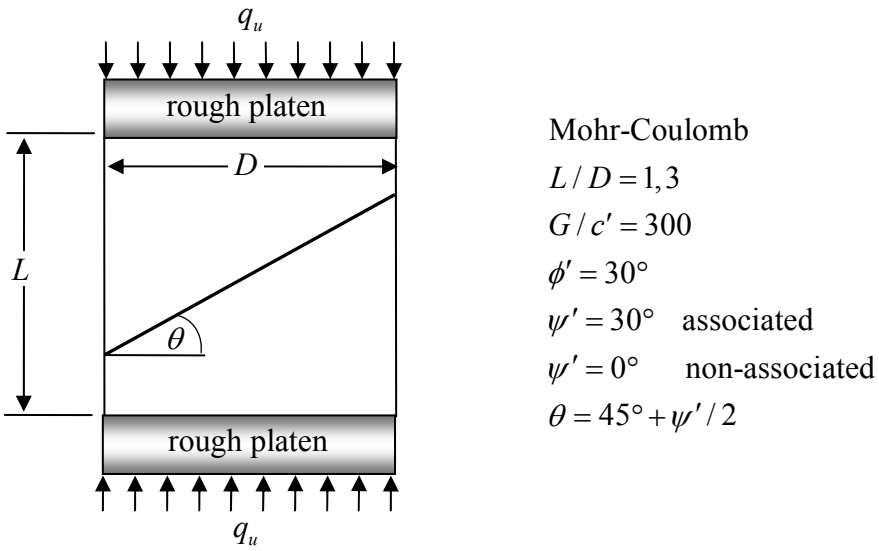

Figure 16 Compression of plane strain block

The nonlinear finite element computer program SNAC (Abbo & Sloan, 2001) is used to analyse this problem for two different L/D ratios (1 and 3) with two different flow rules (associated and non-associated). This code has a number of key refinements for predicting the fully plastic response of geostructures accurately, including automatic stress integration, automatic load stepping, and high order elements such as the highly successful quartic triangle first proposed by Sloan & Randolph (1982). The mesh employed for the case of $L/D = 1$, shown in Figure 17, exploits the symmetry inherent in the problem by considering one quarter of the body and comprises 200 quartic elements. A similar mesh is used for the case of $L/D = 3$, except that the mesh is repeated three times in the vertical direction, giving a total of 600 quartic elements.

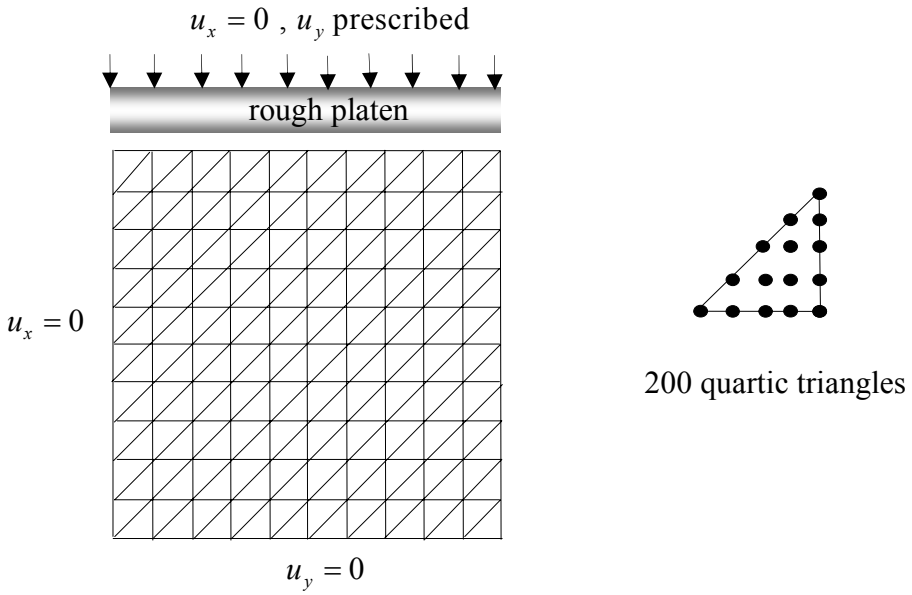

Figure 17 Finite element mesh for compression of plane strain block ($L/D = 1$)

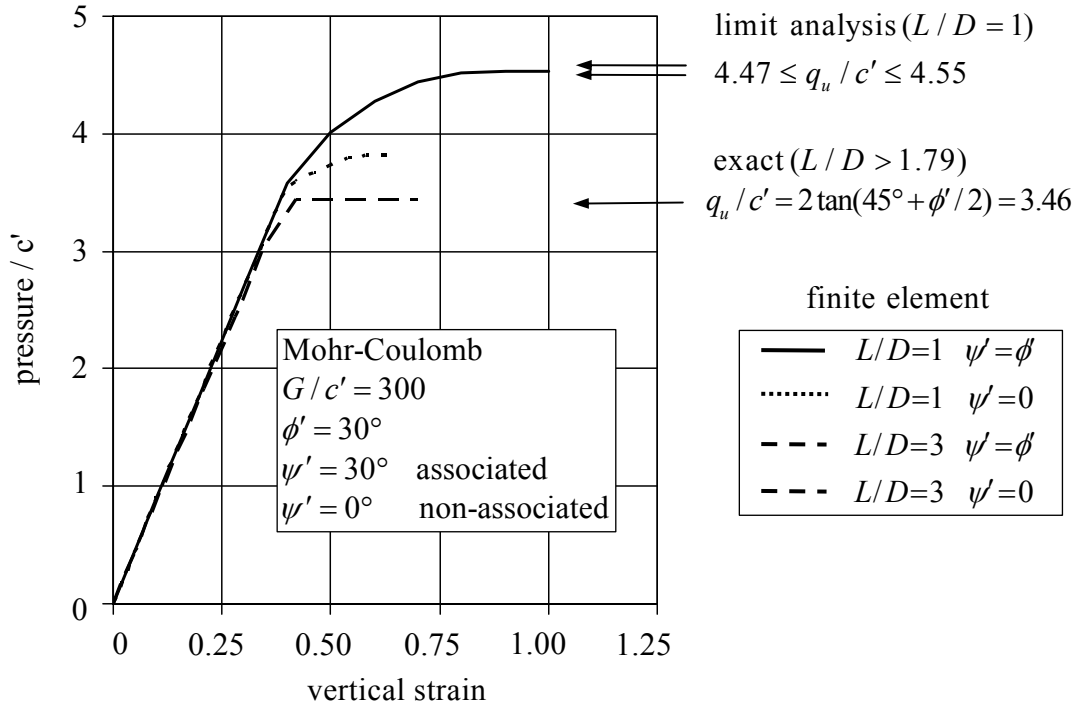

Figure 18 Collapse of plane strain block

The results from the various displacement finite element analyses are shown in Figure 18. For the case of $L/D = 3$, where the failure plane can form freely across the specimen without intersecting the loading platens, the ultimate load is unaffected by the flow rule and agrees precisely with the theoretical value of $q_u/c' = 2\tan(45° + \phi'/2)$. Indeed, the load-deformation plots for the examples with $\psi' = \phi' = 30°$ and $\psi' = 0,\ \phi' = 30°$ are indistinguishable. This confirms the suggestion that, for cases where the degree of kinematic constraint is low, the flow rule will not have a major influence on the collapse load. These results are in stark contrast to those for the short specimen with $L/D = 1$ where the previous failure plane is unable to form without intersecting the end platens, the deformation field is kinematically more constrained, and the limit load for the non-associated flow rule material is about 14% lower than that for the associated case. Unfortunately it is not always possible to quantify the effect of the flow rule in this manner, as non-associated computations for frictional materials with the displacement finite element method are frequently prone to numerical failure, especially when $\psi' \ll \phi'$ (de Borst & Vermeer, 1984).

7 APPLICATIONS

The finite element limit analysis formulations described above are fast and robust and can model cases which include inhomogeneous soils, anisotropy, complex loading, natural discontinuities, complicated boundary conditions, and three dimensions. They not only give the limit load directly, without the need for an incremental analysis, but also bracket the solution from above and below, thereby giving an exact estimate of the mesh discretisation error. These features greatly enhance the practical utility of the bounding theorems, especially in three dimensions where conventional incremental methods are often expensive and difficult to use. Early versions of the finite element limit analysis methods, which were based on linearised yield surfaces and linear optimisation (Sloan, 1988; Sloan, 1989; Sloan & Kleeman, 1995), are suitable for small to medium sized problems and have been used successfully to predict the stability of tunnels (Assadi & Sloan, 1991; Sloan & Assadi, 1991), slopes (Yu *et al.*, 1998), foundations (Merifield *et al.*, 1999; Ukritchon *et*

al., 1998), anchors (Merifield *et al.*, 2001), braced excavations (Ukritchon *et al.*, 2003), and longwall mine workings (Sloan & Assadi, 1994). Later versions of the methods, based on the nonlinear optimisation methods described in this paper, have been used to study sinkhole collapse (Augarde *et al.*, 2003a), tunnel stability (Lyamin & Sloan, 2000), mine stability (Augarde *et al.* 2003b), foundation bearing capacity (Shiau *et al.*, 2003; Salgado *et al.*, 2004; Hjiaj *et al.*, 2004, Hjiaj *et al.* 2005), and anchor capacity (Merifield *et al.*, 2003, 2005).

In this Section we describe some applications of the finite element limit analysis methods to illustrate the types of cases they can model and the results that can be obtained.

7.1 UNDRAINED STABILITY OF A CIRCULAR TUNNEL

The undrained stability of a circular tunnel in clay is an important practical problem that has been studied previously by Davis *et al.* (1980) and Sloan & Assadi (1992). Here we consider the case of a shallow tunnel, of diameter D and cover H, in a soil whose shear strength increases linearly with depth (Figure 19). This idealised problem models a bored tunnel in soft ground where a rigid lining is inserted as the excavation proceeds and the unlined heading, of length L, is supported by an internal pressure σ_t. Collapse of the heading is triggered by the action of the surcharge σ_s and the soil unit weight γ. Although the assumption of plane strain is valid only when $L \gg D$, the stability for this case is more critical than that of a three-dimensional tunnel heading and, therefore, yields a conservative estimate of the loads needed to initiate collapse. For design purposes, the stability of the tunnel is described conveniently by the two dimensionless load parameters $(\sigma_s - \sigma_t)/c_{u0}$ and $\gamma D/c_{u0}$. In practice, as the tunnel is excavated, the unlined heading is supported by either compressed air or clay slurry. This means that, in most design situations, the dimensionless quantities H/D, $\gamma D/c_{u0}$, $\rho D/c_{u0}$ are known and it is necessary to be able to predict the value of $(\sigma_s - \sigma_t)/c_{u0}$ at incipient collapse.

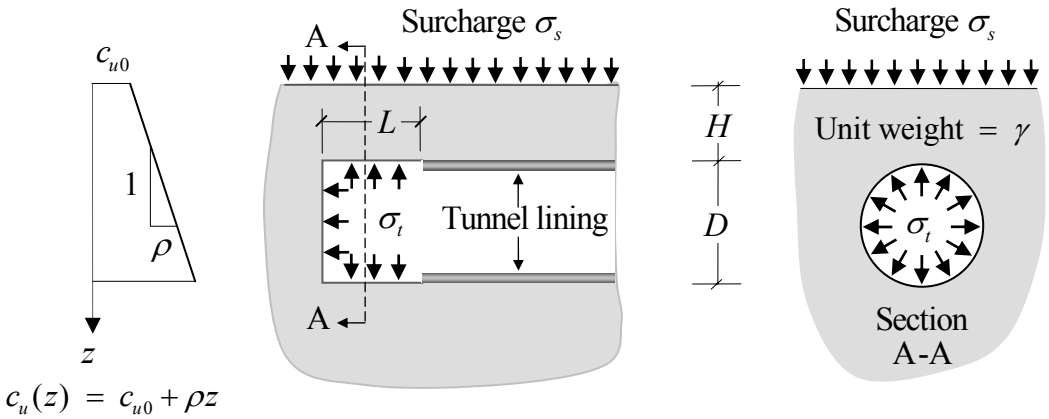

Stability number $(\sigma_s - \sigma_t)/c_{u0} = f\left(H/D,\ \gamma D/c_{u0},\ \rho D/c_{u0}\right)$

Figure 19 Stability of circular tunnel in undrained clay

Figure 20 shows typical meshes that were used for the lower and upper bound limit analysis calculations. In the former case, special extension elements are attached around the border of the grid to extend the statically admissible stress field over the semi-infinite domain. This "completes" the stress field and ensures that the lower bound results are truly rigorous. No such extension is necessary for the upper bound analyses. In both the lower and upper bound grids, discontinuities are present at all edges between adjacent elements, and more than one node can share the same physical co-ordinates. The problem is analysed by fixing c_{u0}, ρ, γ, H, D and σ_s, and then optimising the value of $-\sigma_t$ (i.e. the tensile stress on the face of the tunnel). A Tresca yield criterion is employed to model the behaviour of the clay.

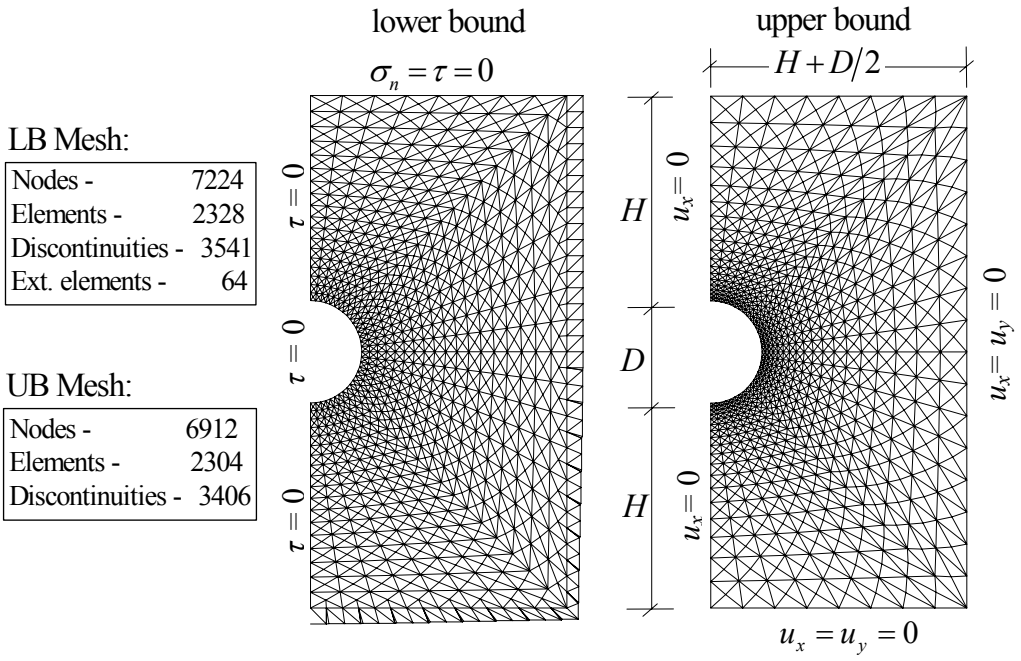

Figure 20 Meshes for circular tunnel in undrained clay

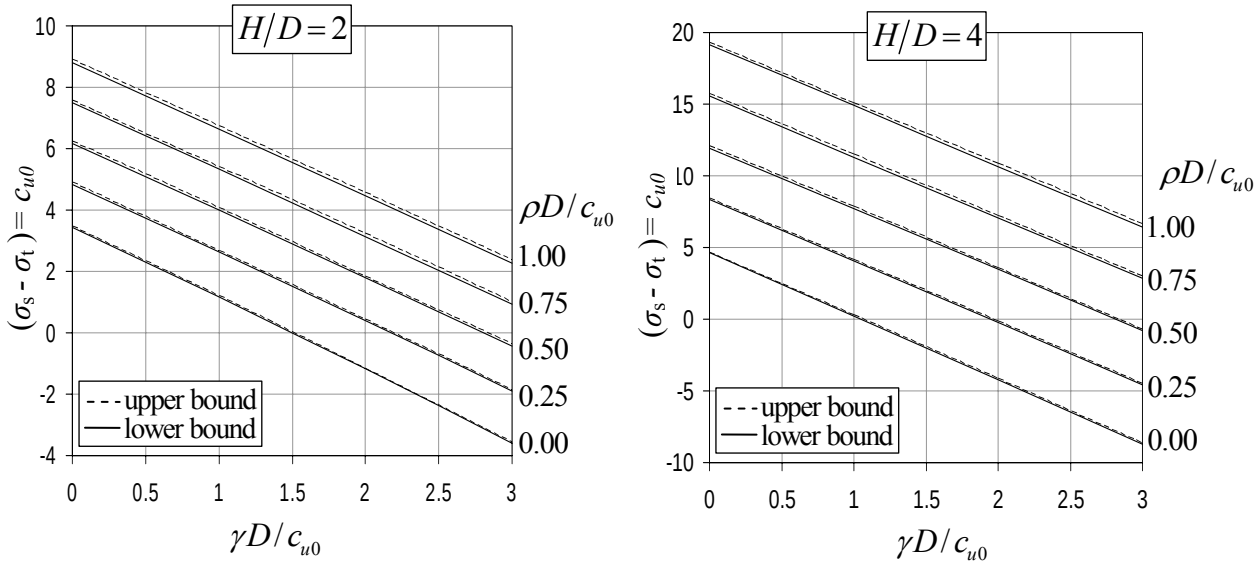

Figure 21 Stability bounds for circular tunnel in undrained clay

Figure 21 shows plots of $(\sigma_s - \sigma_t)/c_{u0}$ as a function of $\gamma D/c_{u0}$ and $\rho D/c_{u0}$ for tunnels with $H/D = 2, 4$. The upper and lower bounds on these stability charts differ by less than 1%, and confirm the ability of the techniques to provide accurate estimates of the limit load. Each analysis required less than 10 seconds on a desktop machine. Figure 22(a) and Figure 22(b) illustrate, respectively, the velocity field and power dissipation at collapse for two tunnels with the same cover and unit weight, but different strength profiles. The failure mechanism for the increasing strength with depth case is clearly shallower and more localised than the failure mechanism for the uniform strength case, and reflects the fact that the soil will always fail in the weakest zones so as to minimise the energy dissipation. The power dissipation contour plots provide a useful insight into the mode of failure, as they highlight the zones where high rates of internal plastic shearing occur.

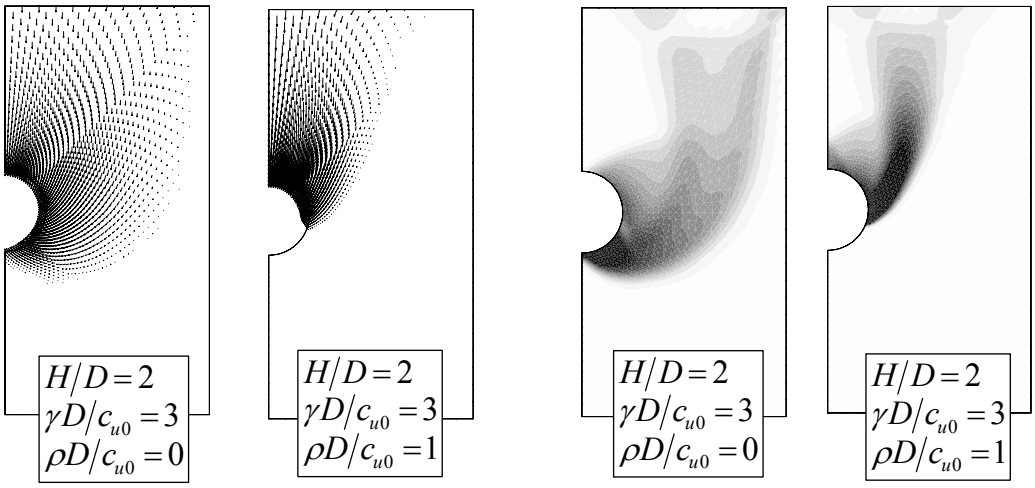

(a) velocity vectors (b) power dissipation

Figure 22 Undrained failure mechanisms for circular tunnel

The detailed centrifuge experiments conducted by Mair (1979) provide an opportunity to compare observed behaviour against the predictions of limit analysis. Some of Mair's results, for the case of a zero surcharge and a clay with a uniform undrained shear strength, are shown in Figure 23. The stability bounds predicted by limit analysis are in excellent agreement with the experimental observations, which show surprisingly little scatter.

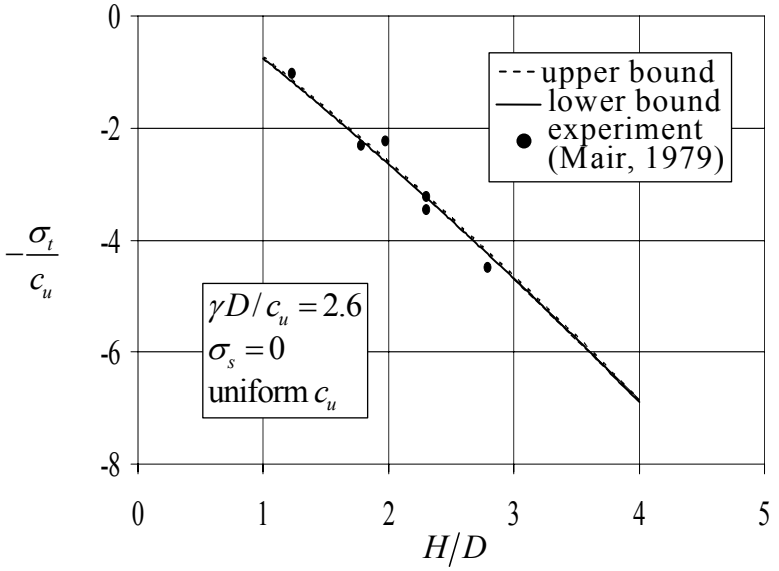

Figure 23 Comparison of theory with centrifuge experiment

7.2 STABILITY OF A SQUARE TUNNEL IN COHESIVE-FRICTIONAL MATERIAL

We now consider the stability of a long unsupported square tunnel in a cohesive-frictional Mohr-Coulomb material, as shown in Figure 24. The tunnel, of dimension D and cover H, is subject to the action of a uniform internal pressure σ_t and self weight γ. The material properties are assumed to be uniform and, for the sake of simplicity, the ground surcharge is taken as zero. Under conditions of plane strain, which are appropriate for a long horizontal tunnel, the stability characteristics are described by the dimensionless quantity σ_t / c'. This stability number is a function of the friction angle ϕ' and the dimensionless parameters H/D and $\gamma D/c'$. The

problem is analysed by fixing c', ϕ', γ, H and D, and then optimising $-\sigma_t$ (the tensile stress on the face of the tunnel).

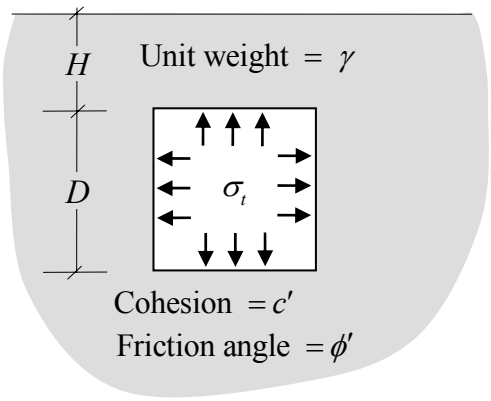

Stability number $-\sigma_t/c' = f\left(\phi', H/D,\ \gamma D/c'\right)$

Figure 24 Square tunnel in cohesive-frictional material

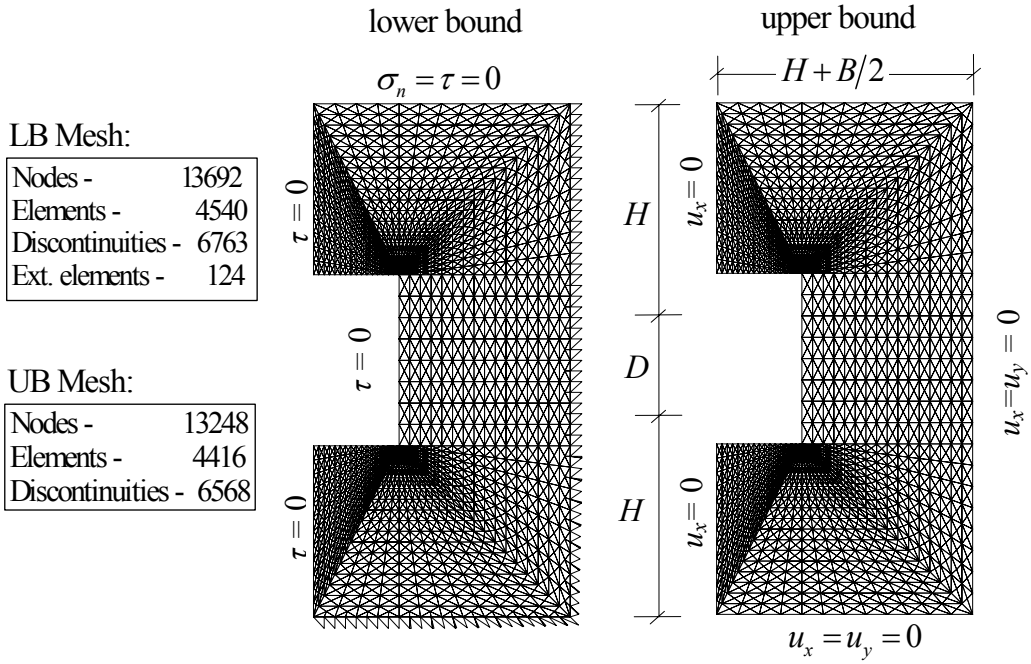

Figure 25 Meshes for square tunnel in cohesive-frictional soil

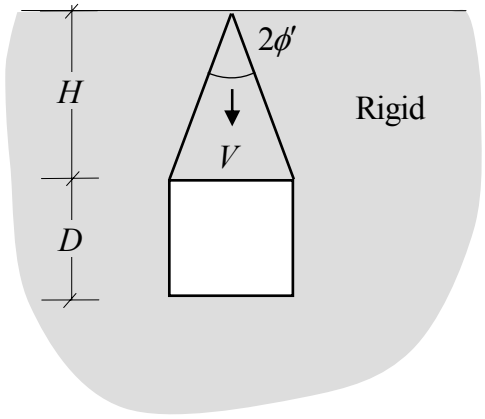

Figure 26 Roof collapse mechanism for square tunnel in cohesive-frictional soil

Typical meshes for the upper and lower bound analyses are shown in Figure 25, while Figure 26 illustrates a simple rigid block failure mechanism. The latter is appropriate for materials with high friction angles, and predicts upper bounds on the limit load that are independent of the tunnel depth (*H/D*). Indeed, equating the rate of work done by the external forces to the internal power dissipated in the two discontinuities gives the upper bound

$$-\sigma_t / c' = (1 - (\gamma D / 4c')) \cot \phi' \tag{16}$$

where we assume that the apex of the failure mechanism does not breach the ground surface so that $H / D \geq \cot \phi' / 2$. Figure 27 shows plots of $-\sigma_t / c'$ as a function of $\gamma D / c'$ and H / D for tunnels with $\phi' = 10°, 40°$. On average, each analysis requires about 30 seconds on a desktop machine and yields upper and lower bounds that bracket the exact solution quite closely. For the cases where $H / D \geq 1$ and $\phi' \geq 30°$, the stability number is largely independent of the tunnel cover and the values predicted by Equation (16) are accurate to within a few percent. This illustrates the benefit of using simple rigid block calculations, not only to check the predictions of numerical methods, but also to provide an understanding of the dominant failure mechanism for a wide range of cases.

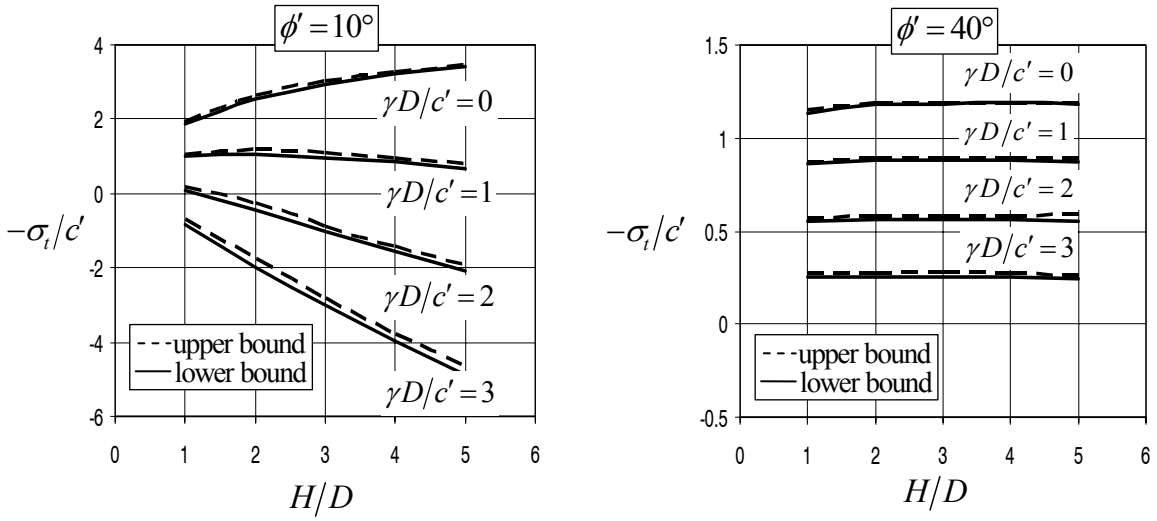

Figure 27 Stability bounds for square tunnel in cohesive-frictional soil

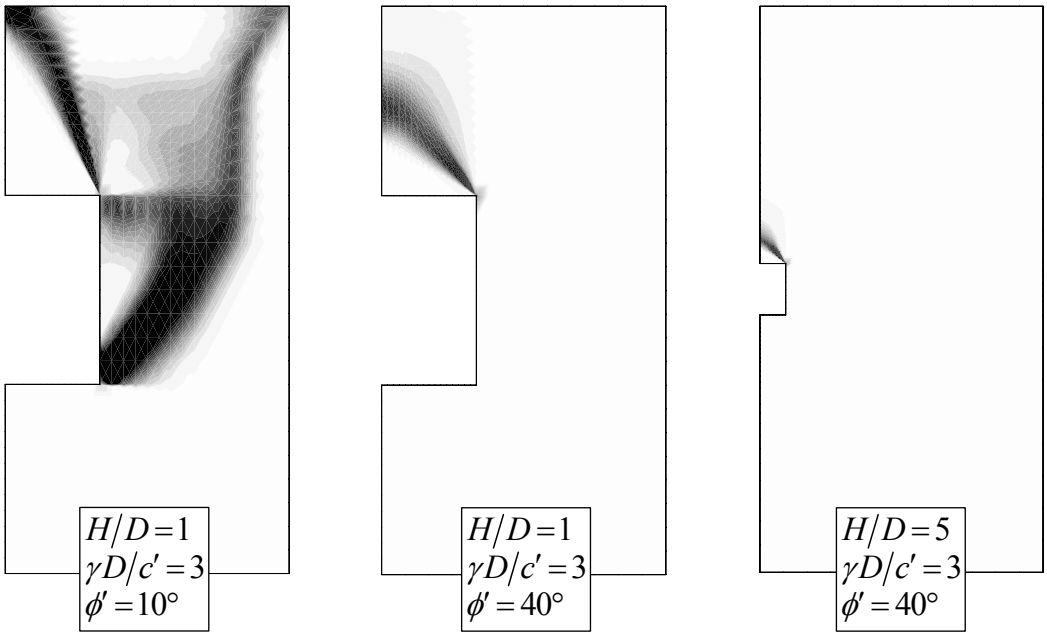

Figure 28 Power dissipation for square tunnel in cohesive-frictional material

Figure 28 illustrates the power dissipation contours at collapse for tunnels with the same unit weight and cohesion, but different friction angles and covers. For shallow tunnels with $H/D=1$, increasing the friction angle from 10° to 40° alters the failure mode dramatically, with the latter case exhibiting a roof collapse mechanism which is very similar to that shown in Figure 26. This type of failure is also clearly evident for a deeper tunnel with $H/D=1$ and $\phi'=40°$.

7.3 STABILITY OF AN UNSUPPORTED CIRCULAR EXCAVATION

We now consider the stability of an unsupported circular excavation, of height H and radius R, in a cohesive-frictional Mohr-Coulomb material (Figure 29). This problem is axisymmetric, but is analysed using a three-dimensional 15° slice as shown in the typical lower bound mesh of Figure 30. Upper bound meshes are similar to those for the lower bound calculations, except that the extension elements are no longer necessary. The governing stability number for this case, $\gamma H/c'$, is a function of both ϕ' and H/R. To perform the bound calculations, the latter quantities are fixed and the former quantity is found by optimising the unit weight.

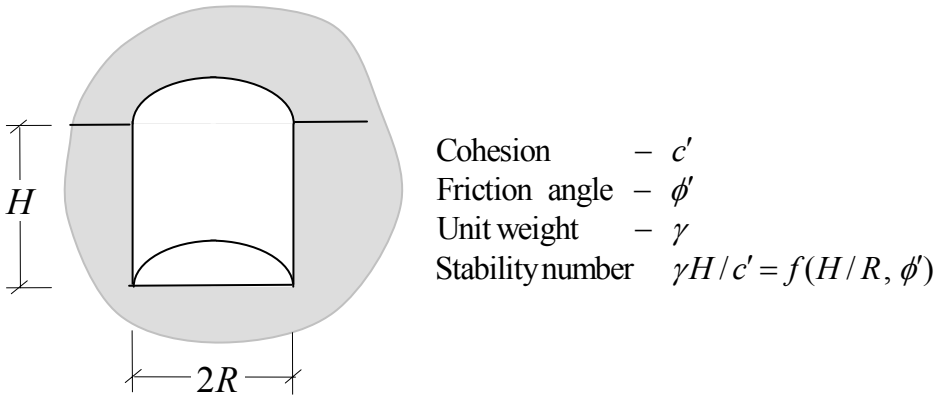

Figure 29 Unsupported circular excavation

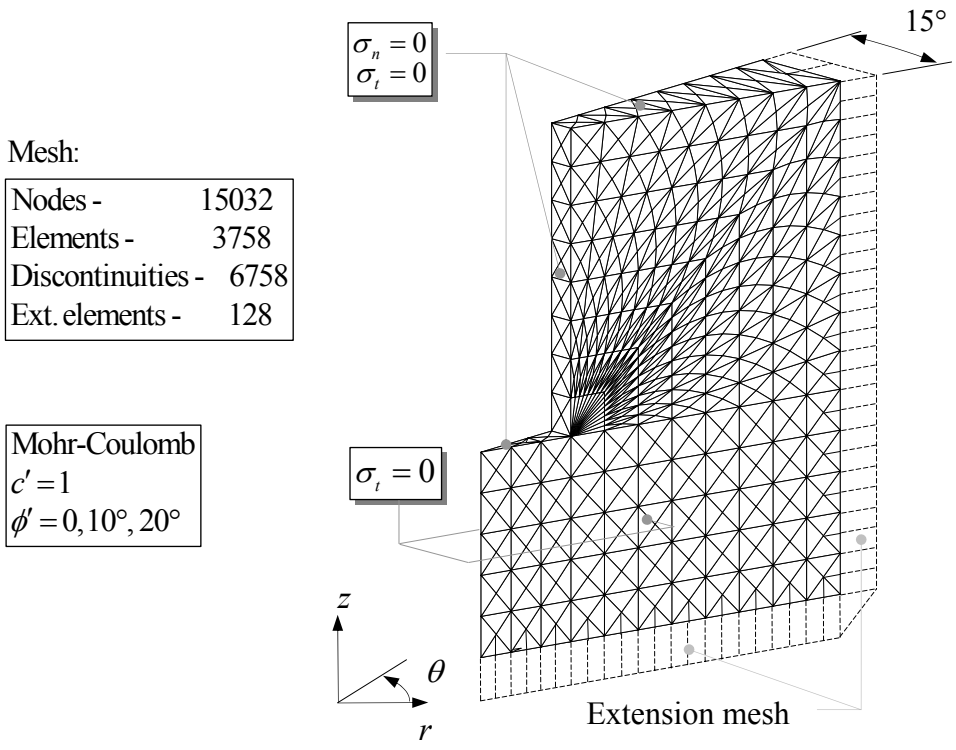

Figure 30 Lower bound mesh and boundary conditions for circular excavation

Limit analysis solutions for the stability number $\gamma H / c'$, shown in Table 1, give upper and lower bounds which differ by a maximum of 2.5%. For the case of a shallow excavation where $H / R = 1$, the agreement is even better with a difference of less than 1%.

Table 1. Stability numbers for unsupported circular excavation

	Stability number $N_s = \gamma H / c'$					
	$H/R=1$		$H/R=2$		$H/R=3$	
ϕ'	LB	UB	LB	UB	LB	UB
0°	5.16	5.19	6.00	6.07	6.65	6.78
10°	6.57	6.60	7.95	8.05	9.11	9.27
20°	8.46	8.53	10.73	10.93	12.79	13.10

Figure 31 plots the lower and upper bound results and, for the purely cohesive case, compares them with those of Britto & Kusakabe (1982), Pastor & Turgeman (1979), and Pastor (1981). Britto & Kusakabe's upper bounds were obtained from an axisymmetric mechanism, while the others were found from finite element formulations of the limit theorems based on linear programming. This comparison confirms the ability of the new methods to provide accurate solutions in three dimensions.

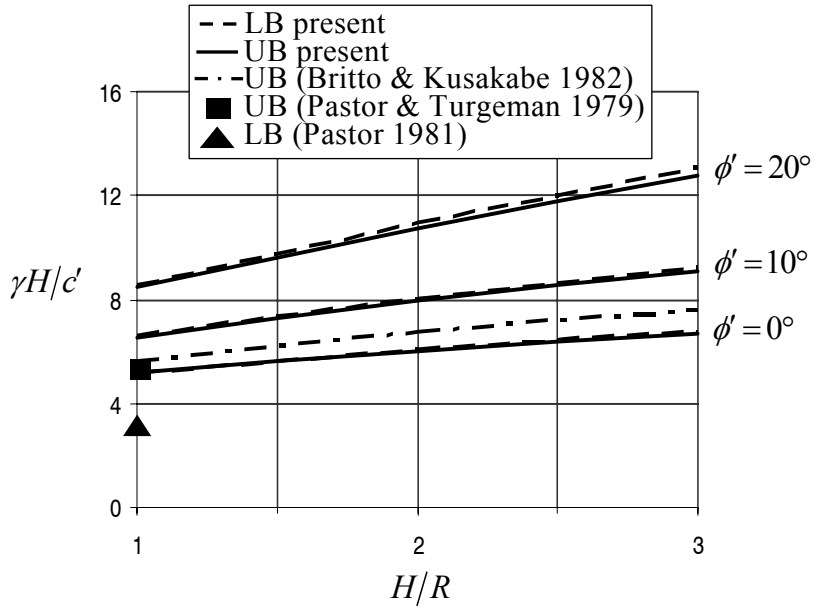

Figure 31 Stability bounds for circular excavation

7.4 UPLIFT CAPACITY OF RECTANGULAR PLATE ANCHORS IN CLAY

Soil anchors are commonly used as foundation systems for structures that require uplift or lateral resistance, such as transmission towers, sheet pile walls, and buried pipelines. Although most plate anchors are usually square, circular or rectangular in shape, existing solutions typically assume a condition of plane strain for simplicity. Close bounds for the case of strip anchors in clay have been obtained by Merifield *et al.* (2001), who applied earlier versions of the finite element limit analysis methods described in this paper. Rigorous solutions for more general anchor shapes are rare, with a notable exception being the treatment of circular anchors by Martin & Randolph (2001). Following Rowe & Davis (1982), anchor behaviour may be divided into two distinct categories; namely those of "immediate breakaway" and "no breakaway". In the immediate breakaway case it is assumed that, under loading, the bottom face of the anchor separates from the surrounding soil and the associated vertical stress is reduced to zero. This corresponds to the situation where there is no

adhesion or suction between the soil and the anchor. In the no breakaway case the opposite is assumed, with the soil/anchor interface sustaining adequate tension to ensure the anchor remains in contact with the soil at all times. This models the case where a substantial adhesion or suction exists between the anchor and the soil. The field behaviour of an anchor is likely to fall somewhere between these two extremes, but it is more conservative to assume that immediate breakaway occurs.

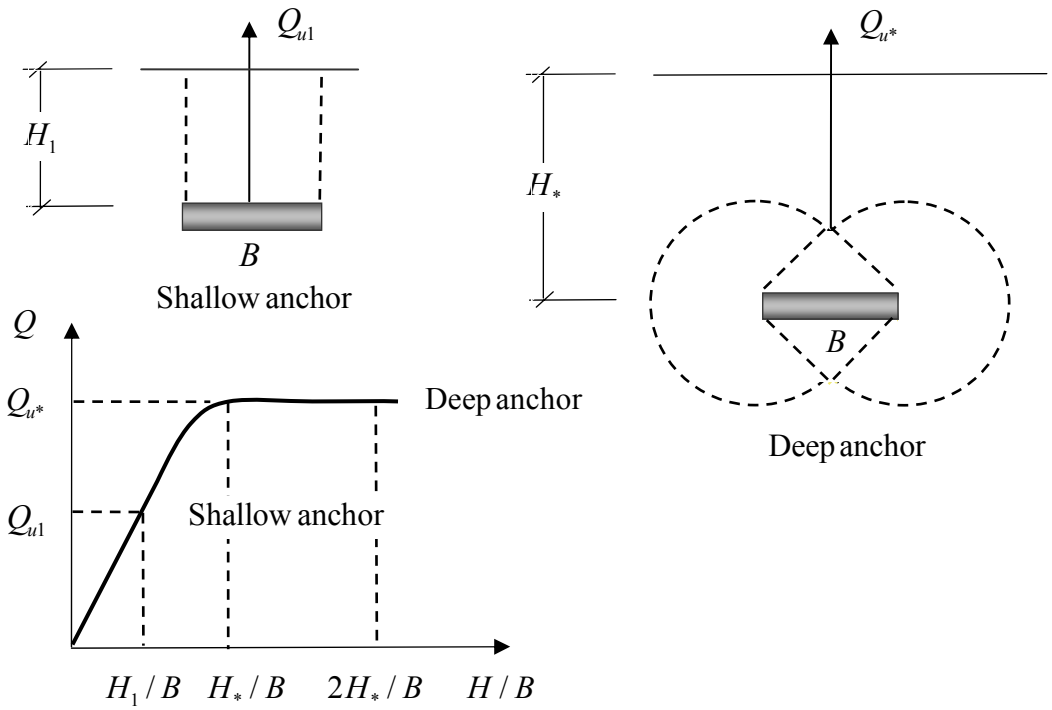

Figure 32 Shallow and deep anchor behaviour

A further complication of anchor behaviour is that it can be classified as either shallow or deep, depending on the mode of failure (Figure 32). An anchor is classified as shallow if, at ultimate collapse, the observed failure mechanism reaches the ground surface. The uplift capacity in this case increases with increasing embedment depth. In contrast, deep anchor behaviour is characterised by localised shear failure around the anchor, so that the uplift capacity becomes independent of the embedment depth. The depth at which the transition between shallow and deep behaviour occurs is known as the critical embedment depth, and is a key design quantity. Burying anchors below the critical embedment depth gives no increase in uplift capacity, but can dramatically increase construction costs.

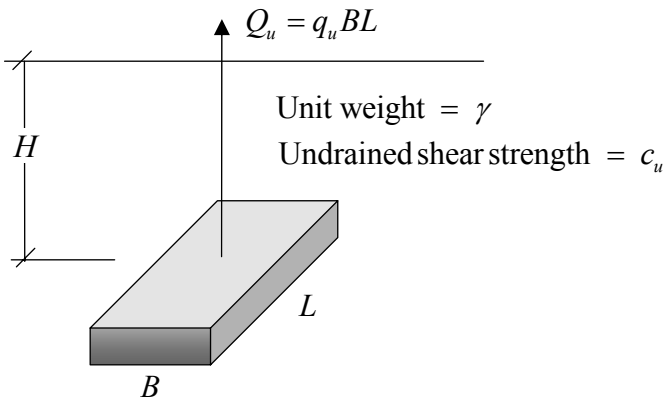

Figure 33 Rectangular plate anchor in clay

We consider here the undrained uplift capacity of a rectangular plate anchor, of width B and length L, buried in clay at a depth H (Figure 33). The soil is modelled using the Tresca yield criterion with a uniform shear strength c_u and unit weight γ. To be conservative, immediate breakaway underneath the anchor is assumed. Under these conditions, the ultimate uplift capacity of the anchor may be written as

$$q_u = N_c c_u + \gamma H \tag{17}$$

where the breakout factor $N_c = (q_u / c_u)_{\gamma=0}$ is a function of $(H/B,\ L/B)$.

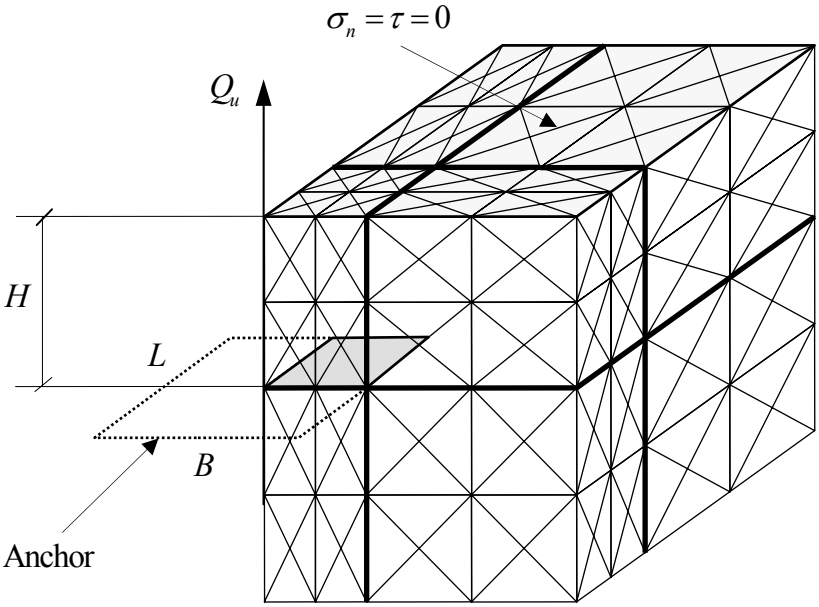

Figure 34 Illustrative mesh for analysis of rectangular anchor in clay

Figure 34 shows an illustrative mesh for the three-dimensional limit analysis calculations (the actual meshes used were much finer than this).

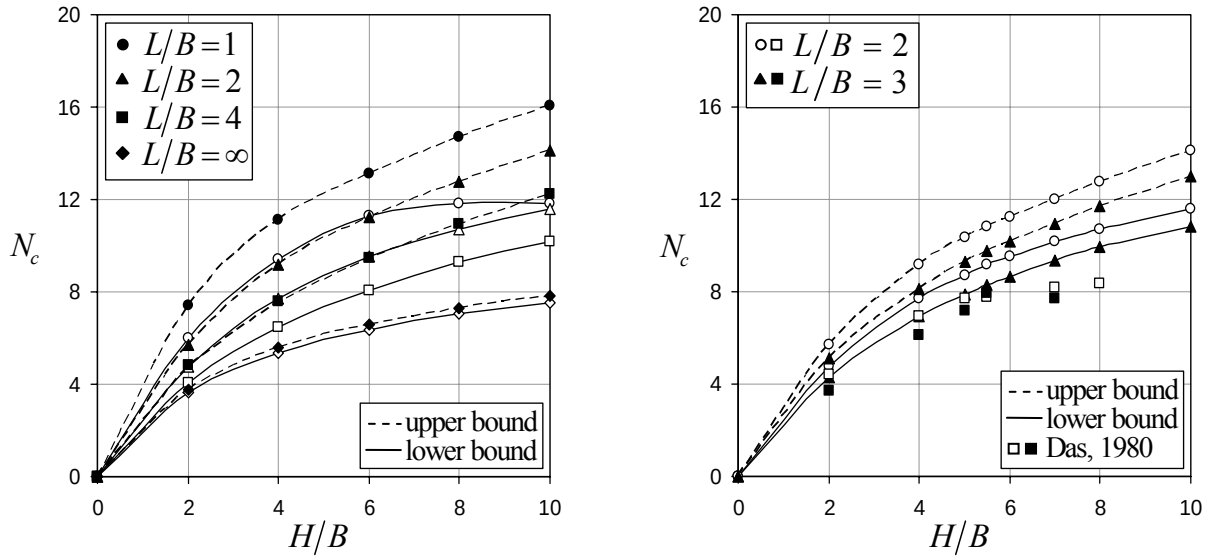

Figure 35 Breakout factors for rectangular anchors

Figure 35 (a) shows plots of N_c versus H/B for various aspect ratios L/B with $\gamma = 0$. For the case of a strip anchor ($L/B = \infty$), the upper and lower bounds bracket the exact breakout factors to

within a few percent. The bounds are less good for the case of square anchor, however, where there is a 25 percent difference at larger embedment depths. This discrepancy is caused by the 2 GB memory limit on our Windows machine, which restricted the number of elements that could be used in the upper and lower bound calculations. Figure 35(b) shows plots of N_c versus H/B for $L/B=2$ and $L/B=3$, and compares the theoretical predictions with the experimental results of Das (1980). The agreement between the two is reasonably good for shallow embedment depths, but is less good for deeper cases. One possible cause for this discrepancy is the large uncertainty associated with controlling and measuring the undrained shear strength in laboratory chamber tests.

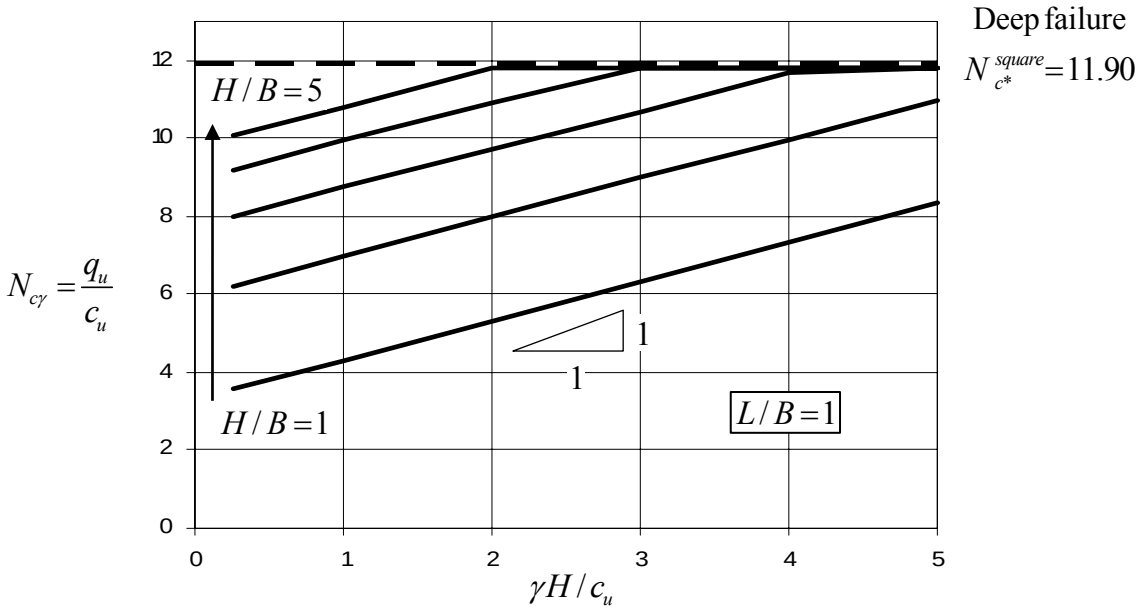

Figure 36 Influence of self weight on breakout factor

To examine the effect of self-weight, Equation (17) can be re-written in the form

$$q_u = N_{c\gamma}\, c_u$$

where $N_{c\gamma} = N_c + \gamma H / c_u$. This indicates that a plot of $N_{c\gamma}$ versus $\gamma H / c_u$ should have a slope of unity. This is confirmed in Figure 36, which shows lower bound results for a square anchor at various depths with various soil unit weights. Note that the uplift capacity does not increase indefinitely and reaches a maximum value $N_{c*} = 11.90$ once the anchor develops a deep failure mode.

To compute the limiting breakout factor N_{c*} for a rectangular footing with an arbitrary L/B ratio, it is sufficiently accurate to use linear interpolation between the values for a square and a strip (Merifield *et al.*, 2003). Assuming that $L/B=10$ gives similar behaviour to that of a strip, this gives

$$N_{c*} = N_{c*}^{strip} + \left(\frac{10 - L/B}{9}\right)\left(N_{c*}^{square} - N_{c*}^{strip}\right)$$

where

$$N_{c*}^{strip} = 11.16$$
$$N_{c*}^{square} = 11.90$$

As discussed by Merifield *et al.* (2003), the results from finite element limit analysis can be used to derive simple design procedures that are based on rigorous theory. For the case of a rectangular anchor in undrained clay, one such procedure is as follows:

(1) Compute N_c from design charts for a given ratios of L/B and H/B.

(2) Compute $N_{c\gamma} = N_c + \gamma H / c_u$.

(3) Compute N_{c*} for given L/B.

(4) If $N_{c\gamma} \geq N_{c*}$ then anchor undergoes a deep mode of failure and $q_u = N_{c*}\, c_u$.

(5) If $N_{c\gamma} < N_{c*}$ then $q_u = N_{c\gamma}\, c_u$

8 CONCLUSIONS

New methods for performing stability analysis in two and three dimensions have been described. The techniques are based on the limit theorems of classical plasticity, finite elements, and nonlinear optimisation, and can be applied to a wide variety of geotechnical problems. Unlike limit equilibrium methods, no assumptions regarding the shape of the failure surface need to be made in advance. Moreover, because the numerical solutions fulfil all the conditions of the limit theorems, the difference between the upper and lower bounds provides a direct estimate of the mesh discretisation error.

9 REFERENCES

Abbo A. J. and Sloan S. W. 2000. SNAC (Solid Nonlinear Analysis Code), *User Manual*, Version 2.0, University of Newcastle, Australia.

Assadi A., Sloan S. W. 1991. Undrained stability of a shallow square tunnel, *Journal of the Geotechnical Division, ASCE*, **117**(8), 1152-1173.

Augarde C. E., Lyamin A. V., Sloan S. W. 2003a. Prediction of undrained sinkhole collapse, *Journal of Geotechnical and Geoenvironmental Engineering, ASCE*, **129**(3), 197-205

Augarde C. E., Lyamin A. V., Sloan S. W. 2003b. Stability of an undrained plane strain heading revisited, *Computers and Geotechnics*, **30**(5), 419-430.

Britto A. M., Kusakabe, O. 1982. Stability of unsupported axisymmetric excavations in soft clay, *Géotechnique*, **32**(3): 261-270.

Coulomb C.A. 1773. Essai sur une application des règles de maximis & minimis à quelques problèmes de statique, relatifs a l'architecture, *Mémoires de Mathèmatique & de Physique présentés à L'Academie Royale des Sciences*, 7, 343-382. (English translation: Note on an Application of the Rules of Maximum and Minimum to Some Statical Problems, Relevant to Architecture, Heyman, J.,Coulomb's Memoir on Statics, An Essay on the *History of Civil Engineering*, Cambridge, Cambridge University Press, 212, 1972).

Das B. M. 1980. A procedure for uplift capacity of foundations in clay, *Soils and Foundations*, 20(1), 77-82.

Davis E. H. 1968. Theories of Plasticity and Failure of Soil Masses. In I. K. Lee (ed.) *Soil Mechanics Selected Topics*, 341-354. Elsevier: New York (USA).

Davis E. H., Gunn M. J., Mair R. J., Seneviratne H. N. 1980. The stability of shallow tunnels and underground openings in cohesive material, *Géotechnique*, **30**, 397-416.

De Borst R, Vermeer P. A. 1984. Possibilities and limitations of finite elements for collapse, *Géotechnique*, **34**(2), 199-210.

Drescher A., Detournay E. 1993. Limit load in translational mechanisms for associative and nonassociative materials, *Géotechnique*, **43**(3), 443-456

Drucker D.C., Greenberg W., Prager W. 1951. The safety factor of an elastic plastic body in plane strain, *Transactions of the ASME, Journal of Applied Mechanics*, **73**, 371-378.

Hjiaj M., Lyamin A. V., Sloan S. W. 2004. Bearing capacity of a cohesive-frictional soil under non-eccentric inclined loading, *Computers and Geotechnics*, **31**(6), 491-516.

Hjiaj M., Lyamin A. V., Sloan S. W. 2005. Numerical limit analysis solutions for the bearing capacity factor N_γ, *International Journal of Solids and Structures*, **42**(5-6), 1681-1704.

Krabbenhøft K., Lyamin A. V., Hjiaj M., Sloan S. W. 2005. A new discontinuous upper bound limit analysis formulation, *International Journal for Numerical Methods in Engineering*, **63**(7), 1069-1083.

Lyamin A. V. 1999. *Three-dimensional Lower Bound Limit Analysis Using Nonlinear Programming*, PhD Thesis, University of Newcastle (Australia).

Lyamin A., Sloan S. W. 2000. Stability of a plane strain circular tunnel in a cohesive-frictional soil. Proceedings J. R. Booker Memorial Symposium, Sydney (Australia), 139-153.

Lyamin A. V., Sloan S. W. 2002a. Lower bound limit analysis using nonlinear programming, *International Journal for Numerical Methods in Engineering*, **55**(5), 573-611.

Lyamin A. V., Sloan S. W. 2002b. Upper bound limit analysis using linear finite elements and nonlinear programming, *International Journal for Numerical and Analytical Methods in Geomechanics*, **26**(2), 181-216.

Lyamin A. V., Krabbenhøft K., Abbo A. J., Sloan S. W. 2005. General approach for modelling discontinuities in limit analysis, Proceedings of IACMAG 2005, Torino (Italy).

Mair R. J. 1979. *Centrifugal Modelling of Tunnel Construction in Soft Clay*, PhD Thesis, University of Cambridge.

Martin C. M., Randolph M. F. (2001). Applications of the lower and upper bound theorems of plasticity to collapse of circular footings, Proceedings of IACMAG 2001, Arizona (USA), 1417-1428.

Merifield R. S., Sloan S. W., Yu H. S. 1999. Rigorous solutions for the bearing capacity of two layered clay soils, *Géotechnique*, **49**(4), 471-490.

Merifield R. S., Sloan S. W., Yu H. S. 2001. Stability of plate anchors in undrained clay, *Géotechnique*, **51**(2), 141-153.

Merifield R. S., Lyamin A. V., Sloan S. W., Yu H. S. 2003. Three-dimensional stability analysis of plate anchors in clay, *Journal of Geotechnical and Geoenvironmental Engineering, ASCE*, **129**(3), 243-253.

Merifield R. S., Lyamin A. V., Sloan S. W. 2005. The stability of inclined plate anchors in purely cohesive soil, *Journal of Geotechnical and Geoenvironmental Engineering, ASCE*, **131**(6), 792-799

Palmer A. C. 1966. A limit theorem for materials with non-associated flow laws, *Journal de Mècanique* , **5**(2), 217-222.

Pastor J. 1981. Analyse limite et stabilite des fouilles', Proceedings, 10th International Conference on Soil Mechanics and Foundation Engineering, Stockholm (Sweden), **3**, 505-508.

Pastor J., Turgeman S. 1979. Formulation linéaire des méthodes de l'analys limite en symétrie axiale, 4th Congrès Francais de Mécanique, Nancy (France).

Prandtl L. 1920. Über die härte plastischer körper, *Göttingen Nachr. Math. Phys. Kl.*, **12**.

Rowe R. K., Davis E. H. 1982. The behaviour of anchor plates in clay, *Géotechnique*, **32**(1), 9-23.

Salgado R., Lyamin A. V., Sloan S. W., Yu H. S. 2004. Two- and three-dimensional bearing capacity of foundations in clay. *Géotechnique*, **54** (5), 297-306.

Shiau S. H., Lyamin A. V., Sloan S. W. 2003. Bearing capacity of a sand layer on clay by finite element limit analysis. *Canadian Geotechnical Journal*, **40**(5), 900-915.

Sloan S. W. 1988. Lower bound limit analysis using finite elements and linear programming, *International Journal for Numerical and Analytical Methods in Geomechanics*, **12**(1), 61-67.

Sloan S.W. 1989. Upper bound limit analysis using finite elements and linear programming, *International Journal for Numerical and Analytical Methods in Geomechanics*, **13**, 263-282.

Sloan S. W., Assadi A. 1991. Undrained stability of a square tunnel in a soil whose strength increases linearly with depth, *Computers and Geotechnics*, **12**(4), 321-346.

Sloan S. W., Assadi A. 1992. The stability of tunnels in soft ground. Proceedings Peter Wroth Memorial Symposium on Predictive Soil Mechanics, Oxford (England), 644-663.

Sloan S. W., Assadi A. 1994. Undrained stability of a plane strain heading, *Canadian Geotechnical Journal*, **31**(3), 443-450.

Sloan S. W., Kleeman P. W. 1995. Upper bound limit analysis with discontinuous velocity fields. *Computer Methods in Applied Mechanics and Engineering*, **127**(1-4), 293-314.

Sloan S. W. and Randolph M. F. 1982. Numerical prediction of collapse loads using finite element methods, *International Journal for Numerical and Analytical Methods in Geomechanics*, **6**(1), 47-76.

Ukritchon B., Whittle A. J., Sloan S. W. 1998. Undrained limit analysis for combined loading of strip footings on clay, *Journal of the Geotechnical and Geoenvironmental Division, ASCE*, **124**(3), 265-276.

Ukritchon B., Whittle A. J., Sloan S. W. 2003. Undrained stability of braced excavations in clay, *Journal of the Geotechnical and Geoenvironmental Division, ASCE*, **129**(8), 738-755.

Yu H. S., Salgado R., Sloan S. W., Kim J. M. 1998. Limit analysis versus limit equilibrium for slope stability, *Journal of the Geotechnical and Geoenvironmental Division, ASCE*, **124**(1), 1-11.